Information Thermodynamics and Fluctuations in Quantum Dots

Barker, David

2022

Document Version:
Other version

Information Thermodynamics and Fluctuations in Quantum Dots

Information Thermodynamics and Fluctuations in Quantum Dots

by David Barker

LUND
UNIVERSITY

DOCTORAL THESIS

Thesis advisors:
Associate Professor Ville F. Maisi
and
Professor Peter Samuelsson

Faculty opponent:
Professor Anne Anthore
Université Paris Cité, France

To be presented, with the permission of the Faculty of Engineering of Lund University, for public criticism in Rydbergssalen at the Department of Physics on Friday, the 9th of December 2022 at 09:15.

Organization
LUND UNIVERSITY

Department of Physics
Box 118
SE–221 00 LUND
Sweden

Document name
DOCTORAL DISSERTATION

Date of disputation
2022-12-09

Sponsoring organization

Author(s)
David Barker

Title and subtitle
Information Thermodynamics and Fluctuations in Quantum Dots

Abstract
In small systems with large fluctuations, the classical description of thermodynamics is no longer sufficient which has led to the development of stochastic thermodynamics. One important result from stochastic thermodynamics is that with measurement and feedback it is possible to use those fluctuations to extract work from a single heat bath coupled to the system. This is thanks to the connection between information and thermodynamics which is the subject of this thesis. Specifically, dissipation and fluctuations have been experimentally studied for thermodynamic processes involving information using a quantum dot system embedded in an InAs nanowire.

Paper I details the fabrication and measurement of double quantum dot devices using the InAs nanowires. Then, in the thesis, the development of real-time readout of the state of the quantum dots using charge sensing is described. In addition, an investigation into the back-action effects of the charge detector was performed.

In Paper II, the work fluctuation-dissipation relation was studied for the operation of the resulting device as a Szilard engine which extracts work from the information about the quantum dot charge state. It was found that as the engine's dissipation decreased, so did its fluctuations.

The results from Paper III show that it is possible to develop and experimentally implement protocols that minimize the dissipation by modifying the shape of the drive used on the system.

Finally, Paper IV investigated a recently discovered thermodynamic uncertainty relation which forces a trade-off between thermodynamic cost and precision. For measurement-feedback scenarios like the Szilard engine, the TUR can be violated unless one also takes into account a time-reversed protocol.

Key words
stochastic thermodynamics, Maxwell's demon, quantum dot, charge sensing, information, feedback

Classification system and/or index terms (if any)

Supplementary bibliographical information

Language
English

ISSN and key title

ISBN
978-91-8039-451-2 (print)
978-91-8039-452-9 (pdf)

Recipient's notes

Number of pages
132

Price

Security classification

Signature _____ Date 2022-10-31

Information Thermodynamics and Fluctuations in Quantum Dots

by David Barker

LUND
UNIVERSITY

Cover illustration front: Heavily processed (for artistic reasons) charge stability diagram of a double quantum dot measured with charge detection.

Faculty of Engineering, Department of Physics
Lund University, Lund, Sweden

ISBN: 978-91-8039-451-2 (print)
ISBN: 978-91-8039-452-9 (pdf)

Printed in Sweden by Media-Tryck, Lund University, Lund 2022

The best that most of us can hope to achieve in physics is simply to misunderstand at a deeper level.
— Wolfgang Pauli

Contents

List of publications

This thesis is based on the following publications, referred to by their Roman numerals:

I **Individually addressable double quantum dots formed with nanowire polytypes and identified by epitaxial markers**
David Barker, Sebastian Lehmann, Luna Namazi, Claes Thelander, Kimberly A. Dick, and Ville F. Maisi
Applied Physics Letters, 114, 183502 (2019)
I fabricated the devices from as-grown nanowires, performed measurements, processed the data and wrote the manuscript all with support from the co-authors.

II **Experimental Verification of the Work Fluctuation-Dissipation Relation for Information-to-Work Conversion**
David Barker, Matteo Scandi, Sebastian Lehmann, Claes Thelander, Kimberly A. Dick, Martí Perarnau-Llobet, and Ville F. Maisi
Physical Review Letters, 128, 040602 (2022)
I developed the fabrication recipe and fabricated the device from as-grown nanowires. I wrote the measurement scripts and performed measurements and data analysis. I wrote the majority of the manuscript with input from the co-authors. M.S. performed the simulations.

III **Constant dissipation rate is optimal for thermodynamic protocols: experimental implementation of Landauer erasure through thermodynamic length**
Matteo Scandi, **David Barker**, Sebastian Lehmann, Kimberly A. Dick, Ville F. Maisi, and Martí Perarnau-Llobet
Submitted
The device is the same as in Paper II, fabricated by me. I wrote the measurement scripts and performed the experiment and most of the data analysis. I wrote the experimental sections of the manuscript with M.S. writing the majority of the rest.

IV **Thermodynamic Uncertainty Relations in an experimentally realized Szilard engine**
David Barker, Sebastian Lehmann, Kimberly A. Dick, Peter Samuelsson, Ville F. Maisi, and Patrick P. Potts
In manuscript
The device is the same as in Paper II and III, fabricated by me. I wrote the measurement scripts and performed the experiment and analyzed the data. I wrote the manuscript with input from the co-authors.

Acknowledgements

Throughout my PhD studies, I've had the great pleasure to get to know so many wonderful people who have contributed to these last five years being great even in the face of a global pandemic. This includes both people I've worked with directly as well as people who have been around making everyday life a bit more enjoyable. I will here try to thank as many people as I can, but making an exhaustive list is most likely impossible. If you're not here, it is most likely a result of me being dumb at the time of writing and not a slight. If you think I missed you, feel free to scribble your own name somewhere in these pages!

The biggest thanks have to go to my main supervisor, Ville. I have learned so much from you and I'm constantly amazed by the depth of your knowledge and curiosity. More than that, you're always focused on building up the community around the science. I feel privileged to have been your first student and I can only imagine great things coming in your career.

Peter, you only officially became my co-supervisor relatively recently, but I feel you were there in spirit before then. You were one of the people I got to have a one-on-one with during my interview and I've always felt comfortable asking you questions when there's something I don't understand.

When I started my studies, it was just Ville and I but we soon grew to a proper group. I have to thank the other group members Antti, Waqar, Harald, and Subhomoy for the great environment in the lab and the group meetings that would sometimes go on for hours simply due to your enthusiasm. I wish you all good luck for the rest of your studies and/or careers!

The work in this thesis would not have been possible without the incredible nanowires grown by Sebastian (from before I even started!). In addition, I need to thank my theory collaborators Martí, Matteo S and Patrick whose work laid the foundation of my own experimental studies. Working closely with theorists has been a real help and I can warmly recommend it to other experimentalists.

I will now give a special shoutout to the people who have shared the space I've spent most of my time for the last five years, namely office B107. Some of you I shared the room with for a long time and some only briefly, but I think you all contributed to the spirit of the office: Frida L, Florinda, Elke, Kristi, Elham, Harald (who moved to B107 and thus forced me to acknowledge him twice), Karthik, and Mado. Our office is full of old relics and the time has come

for me to leave some of my own.

I only started bouldering in the last few months but it's already become a big part of my life and I don't see myself quitting anytime soon. Thanks to the regular climbing group of Simon, Markus A, Stephanie, Max, and Bengt for taking me in when I wanted to start and for continuing to climb with me. Keep sending!

I've already touched on it, but it really is the people who have made FTF such a warm and welcoming place to work, whether they are fellow students, senior researchers or staff. I'll try to thank as many people as I can here for brightening my day-to-day life during lunch-time, fika breaks, after works or retreats: Thanos, David A, Frida E, Julia, Linnéa, Marie, Markus S, Ruby, Mariia, Rubén, Asmita, Anette, Erik, Martin J, Calle, Marcus T, Artis, Damiano, Neimantas, Sudha, Therese, Enrico, Matteo T, Dan, Claes, Martin L, Jason, Adam, the list goes on. Again, add your name if you feel left out (or send me an angry text, I don't mind).

And of course, last but not least I want to thank the H/C corridor gang (they let me in the gang even if I was in the B corridor) who have been some of my closest friends for the last five years: Irene, Sven, Jonatan, Lukas, and Oskar. We have already started to spread across Europe, but I hope we will keep meeting up for more memories!

Populärvetenskaplig sammanfattning

Tidsåldern vi just nu lever i kallas ofta informationstidsåldern tack vare användandet av datorer för att utföra beräkningar och internet för att dela information. Därför är möjligheten att använda energi för att skapa just information en grundpelare för vårt moderna samhälle. Men är den motsatta processen möjlig? Kan man använda information som energikälla? Svaret på den frågan är ja, men det kräver att man har kontroll över små system som är starkt påverkade av fluktuationer från omgivningen. I mitt arbete har jag genomfört sådana processer med kvantprickar - ett system som inte tidigare använts till det syftet. Framförallt har jag varit intresserad av att undersöka hur processen fluktuerar och vad fluktuationerna kan säga om den fysik som ligger bakom.

Energi från information? - Fysikern James Clerk Maxwell introducerade 1867 sitt tankeexperiment "Maxwells demon." Han föreställde sig en tvådelad kammare fylld med en gas. I mitten av kammaren finns en dörr som kan öppnas eller stängas. Vi vet att om gasen bara låts vara så kommer dess temperatur vara densamma på båda sidor om dörren. Enkelt uttryckt betyder det att det kommer finnas ungefär lika många varma (snabba) gaspartiklar som kalla (långsamma) överallt. Vill vi skapa en temperaturskillnad mellan de båda sidorna behöver vi tillföra energi till gasen: detta är hur ett kylskåp fungerar. Här tänkte sig Maxwell istället att om det fanns en varelse (demonen) som kunde mäta hastigheten på enskilda gaspartiklar när de närmar sig dörren kan den sen välja att bara släppa in varma partiklar till den ena sidan och kalla partiklar till den andra. På så sätt kan demonen skapa en temperaturskillnad utan att tillföra någon energi. Det verkar som att informationen demonen får om partiklarna har fyllt samma roll! Självklart kommer den här energin inte från ingenstans, utan en verklig Maxwells demon skulle kräva energi för att utföra de nödvändiga beräkningarna. Eftersom informationen till slut måste raderas fungerar den som ett slags bränsle.

Små system och fluktuationer - För att utföra verkliga experiment med Maxwells demon måste man kunna läsa av och kontrollera väldigt små system. Så små att de blir starkt utsatta för fluktuationer från omgivningen. Ett stort system skulle kunna liknas vid en tung vikt som släpps från en höjd. På sin väg mot marken kommer den ta samma väg varje gång man släpper den. Om man istället släpper ett litet löv från samma höjd så kommer den precis som vikten nå marken till slut. Skillnaden är att lövet kan påverkas av små rörelser i luften och kommer förmodligen aldrig ta exakt samma väg. På samma sätt fungerar ett litet termodynamiskt system: även om man driver det på samma sätt mellan

två punkter kommer mängden energi som krävs för att göra det variera.

Kvantprickar - fällor för elektroner I den här avhandlingen har jag använt mig av så kallade kvantprickar för att skapa små termodynamiska system. Kvantprickar är ytterst små bitar av halvledarmaterial. I mitt fall finns kvantprickarna i *nanotrådar* vars diameter är tiotusen gånger mindre än ett hårstrås. Eftersom de är så små kan bara ett visst antal elektroner få plats eftersom de har samma laddning och därför stöter bort varandra. Vill man trycka in fler elektroner behöver man tillföra energi med hjälp av ett elektriskt fält. Detta gör att man precist kan kontrollera antalet elektroner i en prick. Det går också att ställa in kvantpricken så att antalet elektroner fluktuerar. Man kan i det fallet inte känna till det exakta antalet utan att mäta på kvantpricken. En sådan mätning ger en alltså ny information som kan användas som informationsbränsle.

Chapter 1

Introduction

Thermodynamics is an enduring field of study first developed during the industrial revolution in order to build more efficient steam engines. In such large-scale systems, a description based around averages is sufficient and led to great insights about the nature of energy, heat flow and dissipation. Later, it became clear that for small systems with large fluctuations, such a description is lacking. As technology progressed and machines moved from being room-sized to our modern nanoscale machines, the development of stochastic thermodynamics was necessary. Stochastic thermodynamics moves beyond the description of fluctuations as mere noise, instead studying how they follow their own physical laws which effectively functions as extensions of the well-known laws of thermodynamics. One important consequence of a system's fluctuations is that by gaining information about the system through measurement, it is possible to use feedback in order to extract work when it would seemingly violate the classical laws of thermodynamics. As such, there is an intriguing interplay between information and thermodynamics which lies at the core of this thesis. Specifically, this thesis aims to experimentally investigate the fluctuations in information-driven thermodynamic processes using quantum dot systems embedded in semiconductor nanowires.

Possibly the most important concept in stochastic thermodynamics is the application of thermodynamic quantities to individual trajectories of how single-particle systems evolve over time [1, 2]. Using these definitions, it was possible to derive fluctuation theorems that relate fluctuations between trajectories to the underlying physics of the system itself [3–8]. Experimentally, results from stochastic thermodynamics have been validated since the early 2000s for a number of systems including single molecules [9, 10], colloidal particles [11–13],

single-electron boxes [14, 15] and quantum dots [16–18].

The connection between information and thermodynamics was first established by Maxwell in 1867, in his famous Maxwell's demon thought experiment [19] where he argues that by measuring on the individual particles of a gas, it would be possible to violate the second law of thermodynamics. Later on, it was understood that by including the thermodynamic cost of processing the information gained in the measurement, the second law was restored [20, 21]. However, the concept of using information to extract work was an intriguing one, so theoretical work continued. Eventually, the fluctuation theorems developed in stochastic thermodynamics were generalized to account for the effect of information and feedback [22–24]. Due to the need to both measure and control single-particle systems, no experimental implementations were done until technology had matured in the 2010s, but the concept has since been demonstrated with colloidal particles [25, 26], single-electron boxes [27, 28] and DNA-pulling experiments [29]. Most of the experimental work done so far has focused on achieving high information-to-work conversion efficiency. Only very recently have the fluctuations in inormation-to-work conversion processes been studied experimentally, which includes the work in this thesis.

The systems studied in this thesis are single electrons in semiconductor quantum dots. If a piece of semiconductor is very short in one dimension, electrons will be confined in that direction. If they are confined in all three spatial dimensions, a quantum dot is formed. Due to Coulomb interactions, a quantum dot can be loaded with a discrete, well-defined number of electrons. Furthermore, the density of states of zero-dimensional semiconductor systems means that the electrons in a quantum dot take on discrete energy levels. As such, quantum dots provide an excellent model system for stochastic thermodynamics. The quantum dots used in this thesis were formed in semiconductor nanowires, which are rods of material less than 100 nm in diameter. The nanowires allow for fully material-defined quantum dots to be formed, since electrons will already be confined in two dimensions due to the shape of the nanowire. The final degree of confinement comes in the shape of polytype engineering, where a bandgap mismatch between two crystal phases create potential barriers [30–32] for electrons.

The work in the thesis is collected in the four papers I-IV. The development of devices with such nanowire quantum dot systems is described in Paper I. Then, Papers II, III, and IV all consist of experimental studies of information thermodynamics, with a focus on fluctuations and dissipation. The rest of the thesis is structured as follows: in Chapter 2, the main concepts of stochastic thermodynamics are introduced, following a brief description of traditional thermody-

namics. In addition, the connection between thermodynamics and information is described. In particular, the Szilard engine thought experiment is described in detail. Chapter 3 introduces the systems and methods used in the thesis work. Using the constant interaction model, characteristics of both single and double quantum dot systems are explained. The chapter then moves into the specific material system and fabrication methods used for the devices (while giving a summary of Paper I). Finally, the very important charge sensing technique is described. In Chapter 4, the thermodynamic concepts introduced in Chapter 2 are connected and applied to the device architecture described in Chapter 3. Following that, Papers II, III, and IV (which all used the same device) are summarized. Concluding the thesis is Chapter 5 which functions as a summary as well as an outlook over possible future directions.

Chapter 2

Thermodynamics

This chapter introduces the thermodynamic concepts that lie at the heart of the work in this thesis. First, the laws of classical thermodynamics for macroscopic systems are presented. Then, a description of those concepts are explained in terms of statistical mechanics which brings the chapter closer to a microscopic picture. From there, an introduction to stochastic thermodynamics on the trajectory level is given, together with some important results. The effect of information and feedback on thermodynamic systems concludes the chapter.

1 From classical to stochastic thermodynamics

1.1 The laws of thermodynamics

Traditional thermodynamics is a phenomenological theory which was developed in order to understand and improve heat engines. As such, it considers macroscopic systems containing a very large number of particles. Furthermore, it only deals with systems at or near equilibrium. Nevertheless, it is an excellent starting point for describing heat, work, and temperature. The theory revolves around the *laws of thermodynamics*, which will be briefly reviewed in the following. A more complete picture can be found in, for instance, the textbook by Kondepudi and Prigogine [33].

The internal energy U of a closed system can be changed either by a work contribution W from some external parameter or by exchanging heat Q with a heat reservoir. U is known as a *state function* which characterizes the state itself.

On the other hand, Q and W depend on the way the system reached its state and are called *path functions*. However, the total energy must be conserved, so that for small changes

$$\mathrm{d}U = \mathrm{d}W + \mathrm{d}Q. \tag{2.1}$$

Equation (2.1) expresses the *first law*. Note that the first law only describes what happens to the energy in any given process, but does not address which processes are possible. To describe this, the concept of *entropy* is introduced. The entropy, S, of a system is a state function that broadly speaking characterizes the degree of its disorder. The *second law* states that the entropy of a closed system can never decrease, i.e.

$$\mathrm{d}S \geq 0. \tag{2.2}$$

If the system is in contact with a heat reservoir (which maintains equilibrium even when exchanging heat), it is the entropy of the combined system S_{tot} that can not decrease:

$$\mathrm{d}S_{tot} = \mathrm{d}S + \mathrm{d}S_r \geq 0, \tag{2.3}$$

where the subscript r indicates the reservoir. For the reservoir itself, its temperature T is the proportionality constant between its energy and entropy so that $\mathrm{d}E_r = T\mathrm{d}S_r$. Since a heat reservoir only exchanges energy through heat, we further get $\mathrm{d}Q_r = T\mathrm{d}S_r$ and finally (noting that $\mathrm{d}Q_r = -\mathrm{d}Q$)

$$\mathrm{dS} \geq \frac{\mathrm{d}Q}{T}. \tag{2.4}$$

For a reversible process, equality is achieved in equation (2.4). Another important consequence of the second law requires the introduction of an additional state function: the *Helmholtz free energy* $F = U - TS$. Then, for a process that takes the system from one equilibrium state to another, $\Delta F = \Delta U - T\Delta S$. Combining this with equations (2.1) and (2.4), yields an inequality for the amount of work needed to perform the transition:

$$W \geq \Delta F, \tag{2.5}$$

where equality again indicates a reversible process. If $\Delta F \leq 0$, equation (2.5) provides a bound for the amount of work that can be extracted in the process. The discussion of the second law ends here with a final formulation which is very important in the context of this thesis, namely the Kelvin-Planck statement: *"It is impossible to construct a device which operates on a cycle and produces no other effect than the production of work and the transfer of heat from a single body"*. Such a device would be a perpetual motion machine, which is thus forbidden by the second law of thermodynamics.

There are two further laws, which are included here for completeness but not extensively discussed in the thesis. First is the *third law*, which states that there is a temperature of absolute zero where the entropy of a perfect crystal will also be zero. Finally, the sometimes included *zeroth law of thermodynamics* states that if one system is in equilibrium with two others, those two systems must also be in equilibrium with each other.

1.2 The statistical mechanics picture

In order to understand the thermodynamics of small systems, it is helpful to first consider macroscopic systems through a microscopic lens. A macroscopic system consists of a number of microscopic states i with energy levels U_i and probability distribution p_i so that $\sum_i p_i = 1$. Any function of the system can now be given as an ensemble average of the corresponding microstate function. For example, the internal energy is:

$$U = \langle U \rangle = \sum_i U_i p_i. \tag{2.6}$$

For a small change in energy $\mathrm{d}U$,

$$\mathrm{d}U = \sum_i (\mathrm{d}U_i p_i + U_i \mathrm{d}p_i). \tag{2.7}$$

Identifying $\sum_i \mathrm{d}U_i p_i$ as a work contribution $\mathrm{d}W$ (the energy levels are moved) and $\sum_i U_i \mathrm{d}p_i$ as a heat contribution $\mathrm{d}Q$ (occupation probability is changed by jumping between microstates with different energy), the first law is re-obtained.

As an example distribution, we look again at a system coupled to a heat reservoir. In that case, its (equilibrium) distribution is known as the *canonical distribution*:

$$p_i = \exp\left[-\frac{1}{k_B T}(U_i - F)\right], \tag{2.8}$$

where F is the *Helmholtz free energy* and k_B is Boltzmann's constant.
In this framework, entropy is defined by the *Gibbs entropy*:

$$S = -k_B \sum_i p_i \ln p_i, \tag{2.9}$$

which in combination with the above definition of $\mathrm{d}Q$ can reproduce the relation $\mathrm{d}S = \mathrm{d}Q/T$ for systems near equilibrium in contact with a thermal reservoir. In addition, using the canonical distribution of equation (2.8), the standard expression for the Helmholtz free energy $F = U - TS$ can also be acquired.

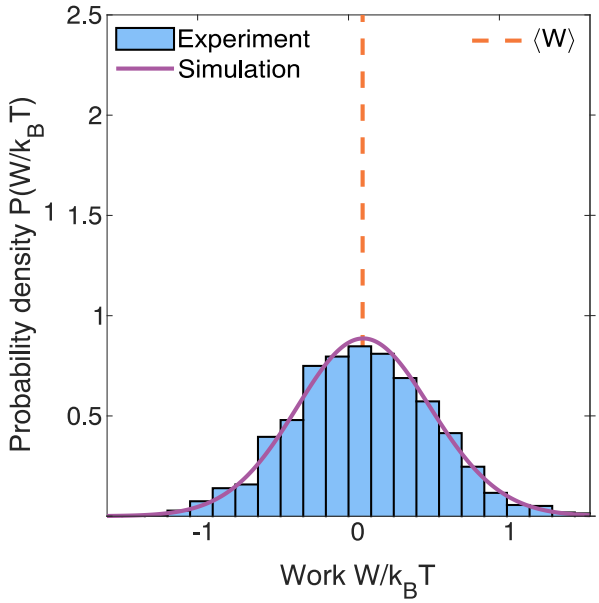

Figure 2.1: An example of a distribution of the work needed to lift and then lower an electronic energy level in contact with a reservoir. On average it requires some work $\langle W \rangle$, but in individual trajectories the work may take on values higher or lower (and sometimes work is even extracted). In this particular example, the energy level is an electronic state in a quantum dot in an InAs nanowire. The level is manipulated by an external gate voltage.

1.3 Trajectory thermodynamics

As seen in section 1.2, the laws of thermodynamics arise from ensemble averages of microstates. However, there is an underlying assumption that the deviations from the average are small, which is true for most macroscopic systems. But what if the system is so small that such fluctuations can no longer be neglected? An extreme of such a system would be individual microscopic particles but also holds true for systems like molecular motors or Brownian motion particles. One important consequence of the fluctuations is that thermodynamic quantities do not take on single values, but are stochastic quantities which follow a distribution (for an example, see Figure 2.1). This section gives a brief introduction to concepts of stochastic dynamics on the level of individual trajectories, and more exhaustive descriptions can be found in reviews such as those written by Jarzynski [1] and Seifert [2].

Consider a system with microstates i described by some probability distribution p_i. A trajectory is defined as the evolution of the system over time, here denoted $x(t, \lambda)$, where λ is some external control parameter which drives the system. During the trajectory, the control parameter can shift both the energy

of a state as well as the probability distribution. The energy of the system at any given time is then simply the energy of the individual microstate the system holds at that instant, i.e. $U = U_i(\lambda(t))$. For a trajectory x between times t_0 and t_f, the energy difference only depends on the state at the beginning and end, $\Delta U(x) = U_i(t_f) - U_i(t_0)$. For the sake of simplicity, any quantity will be assumed to be given at the trajectory level in the rest of this section, so that $\Delta U(x) = \Delta U$. The first law of thermodynamics must still hold for each trajectory:

$$\Delta U = W + Q. \tag{2.10}$$

How are work W and heat Q then defined on the trajectory level? Keep in mind that the trajectory is defined both by which state it is in and how those states evolve over time. Any trajectory will then contain a number of "jumps" at times $t_1, t_2, \ldots, t_N$. Work is defined by how much the energy of the states are shifted by the control parameter while the system is in that state.

$$W = [EU_{i1}(t_1) - U_{i0}(t_0)] + [U_{i,2}(t_2) - U_{i1}(t_1)] + \ldots + [U_{if}(t_f) - U_{iN}(t_N)] \tag{2.11}$$

where the subscript iN indicates the state of the system after the Nth jump. Heat, on the other hand arises from jumps between states of different energy. Summing over all the jumps throughout the trajectory gives

$$Q = \sum_{j=1}^{N} \left[U_{ij}(t_j) - U_{ij-1}(t_j) \right]. \tag{2.12}$$

As outlined above, there is no issue describing quantities like energy, work and heat on a trajectory level but what about entropy? Previously it has been related to the disorder of an ensemble, but that clearly is not possible in this case. Instead, the stochastic entropy is related to the likelihood of finding the system in state i [34]:

$$S = S_i(\lambda(t)) = -k_B \ln p_i(t), \tag{2.13}$$

and for the entropy change over a trajectory

$$\Delta S = k_B \ln \frac{p_0(t_0)}{p_f(t_f)}. \tag{2.14}$$

Note that ΔS can be non-negative even if the system does not change its state. In addition to this stochastic entropy change of the system, there is also the entropy change in the environment ΔS_{env}. For a system coupled to a heat

reservoir which is given heat Q_r over the trajectory, $\Delta S_{env} = Q_r/T$. The total entropy produced over the trajectory is thus given by

$$\Delta S_{tot}(x) = \frac{Q_r(x)}{T} + k_B \ln \frac{p_0(t_0)}{p_f(t_f)}. \tag{2.15}$$

In contrast to the macroscopic case, this quantity can take on any sign. However, on average $\langle \Delta S_{tot} \rangle \geq 0$, restoring the second law of thermodynamics. In the same way, the second law formulation of Equation (2.5) is given by $\langle W \rangle \geq \Delta F$.

2 Fluctuation theorems

As described above, the second law of thermodynamics is closely related to the idea of reversibility. Traditionally, irreversible processes are described by inequalities such as Equation (2.5), with equalities being reserved for reversible ones. However, stochastic thermodynamics allows for the construction of stronger statements by taking into account fluctuations. For a system in contact with a heat reservoir that is driven from a point where it is in equilibrium to a point where it is not necessarily in equilibrium, Jarzynski managed to derive the *Jarzynski equality* (JE) [3]:

$$\exp\left(-\frac{\Delta F}{k_B T}\right) = \left\langle \exp\left(-\frac{W}{k_B T}\right) \right\rangle. \tag{2.16}$$

Note that ΔF here is the difference in free energy between the two corresponding equilibrium states, while W is the work done to the system in a non-equilibrium process. The implication is that by performing an ensemble of non-equilibrium measurements, one can extract information about equilibrium quantities which is a key result in stochastic thermodynamics. Through Jensen's inequality, the JE also implies the second law bound $\langle W \rangle \geq \Delta F$. Furthermore, for slowly driven systems near equilibrium, the distribution of W is Gaussian. In those cases, the Jarzynski equality implies a *fluctuation-dissipation relation* (FDR) [3, 35]:

$$W_{diss} = \frac{\sigma_W^2}{2 k_B T}, \tag{2.17}$$

where W_{diss} is the work dissipated in the process given by $W_{diss} = W - \Delta F$. Since the JE involves an average over trajectories, it is known as an *integral fluctuation theorem* (IFT) of which there exists a wider class.

In addition to IFTs, there is another type of fluctuation theorem known as

detailed fluctuation theorems which relates probabilities in processes to probabilities in their corresponding backward processes. For every trajectory that evolves from $t = 0$ to $t = \tau$ with control parameter $\lambda(t)$, a backward process takes the system in the opposite direction using the time-reversed control parameter $\lambda_B(\tau - t)$. If both the forward and backward processes are initially at equilibrium, the *Crooks fluctuation theorem* [5, 6] says that

$$\frac{P(W)}{P_B(-W)} = \exp\left(\frac{W - \Delta F}{k_B T}\right), \tag{2.18}$$

where $P(W)$ and $P_B(-W)$ are the work distributions in the forward and backward process, respectively. For a reversible process, $P(W) = P_B(-W)$. Furthermore, one can consider time-symmetric processes ones where $\lambda(t) = \lambda_B(\tau - t)$ and the initial state is equivalent to the final state. For such processes, obviously the two work distributions are identical as well.

The JE and CFT are two important examples of fluctuation theorems that relate work and free energy, expanding upon the second law of thermodynamics in small systems. They were first demonstrated experimentally in the early 2000s and have since been applied to a variety of systems, such as DNA hairpins [9, 10], single electron boxes [14], mechanical resonators [36, 37] and colloidal particles [13]. Note that they both belong to larger classes of relations which relate different thermodynamic quantities, such as entropy production [38, 39].

3 Thermodynamic uncertainty relations

Recall how stochastic thermodynamic quantities take on a distribution that can be experimentally accessible by recording a great number of individual trajectories. For an arbitrary quantity ϕ, this distribution can be characterized by its mean $\langle\phi\rangle$ and its variance σ_ϕ^2. In 2015, Barato and Seifert showed that the ratio of these are bounded by the average entropy produced $\langle\Delta S\rangle$ [40]:

$$\frac{\sigma_\phi^2}{\langle\phi\rangle^2} \geq \frac{2k_B}{\langle\Delta S\rangle}. \tag{2.19}$$

Since Equation (3) constitutes a trade-off between thermodynamic precision and thermodynamic cost (entropy production), it has come to be called a *thermodynamic uncertainty relation* (TUR). It provides the possibility to infer thermodynamic quantities by studying fluctuating currents in nanoscale systems [41]. As an example of applications, using the TUR allowed for derivation of a tighter

bound for the efficiencies of molecular motors than what was provided by the second law of thermodynamics [42]. The TUR gained much attention in the theory community and was applied to a number of other systems such as heat engines [43] and Brownian clocks [44]. Note that the TUR in Equation (3) was derived for quite limited conditions. This may not always be a downside. For example, due to its dependency on classical physics, it has been proposed that it can be used as an indicator for quantum effects in systems [45]. However, due to the constraints there is also a significant ongoing effort to develop new TURs and expand their applicability [46]. Notably, it has been generalized to both periodically driven systems [47, 48] as well as systems driven in finite time [49].

Crucially, the above mentioned TURs do not apply to systems with broken time-reversal symmetry such as ones with magnetic hysteresis or, especially interesting in the context of this thesis, processes involving measurement and feedback. In these cases, TURs need to be derived that take into account thermodynamic quantities both in a forward trajectory as well as a time-reversed trajectory. The TUR then provides bounds for this "symmetrized" quantity. For example, the following TUR was derived for measurement-feedback scenarios [50]:

$$\frac{\sigma_\phi^2 + \sigma_{\phi,B}^2}{(\langle\phi\rangle + \langle\phi\rangle_B)^2} \geq \frac{1}{\exp\left(\frac{\langle\Delta S_I\rangle + \langle\Delta S_I\rangle_B}{2k_B}\right) - 1}, \tag{2.20}$$

where the subscript B corresponds to quantities in the time-reversed process. In addition, a term I to account for the information gained in the measurement step needs to be added to the entropy production term so that $\Delta S_I = \Delta S + I$. That is due to the deep link between information and thermodynamics which will be explored in more detail in the upcoming Section 4.

While TURs have already been studied quite extensively in theory, there are few experimental studies. Pietzonka et al. illustrated the finite time-generalization of the TUR using a colloidal particle in an optical trap [49]. A similar platform was used by Paneru et al. to implement a feedback system which showed the expected violation of both equation and a number of generalized versions [51]. They were, however not able to test equation 2.20 experimentally. Finally, Pal et al. used nuclear magnetic resonance to test a number of TURs [52].

4 Thermodynamics and information

4.1 Maxwell's demon

It is not obvious that there would be a link between information and thermodynamics. The first such link came in the form of a thought experiment by James Maxwell in order to demonstrate that the second law of thermodynamics is only a statistical principle [19]. The thought experiment is sketched in Figure 2.2. He imagined two boxes, A and B, filled with a gas and connected by a shutter that can be opened or closed. Then, an intelligent being (later named Maxwell's demon) would measure the velocity of molecules approaching the shutter. If the molecule came from the A side and was slower than the average molecule in B, the demon would open the shutter and let it through. Likewise, if it came from B and was faster than the average molecule in A it would go through. Thus, A would eventually contain a hotter gas than B despite no work having been performed on the system. Thus, by the demon gaining information about the system, the second law of thermodynamics is seemingly violated.

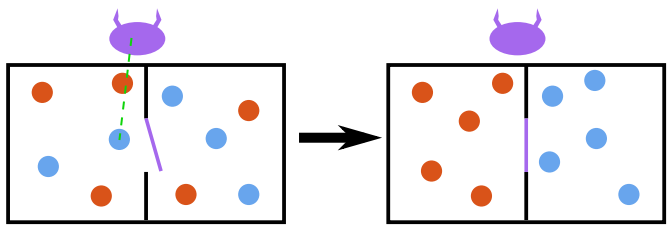

Figure 2.2: Schematic of Maxwell's demon. Here, blue dots represent slow particles and red dots represent fast particles. The demon measures the velocity as the approach the shutter and then decides whether to let the particle through. In the end, it has created a temperature gradient.

4.2 Szilard's engine

In 1929, the link between information and thermodynamics was quantified by Leo Szilard [53]. He conceived of a heat engine using a single-molecule gas and a Maxwell's demon. The engine operation is illustrated in Figure 2.3. First, the molecule is placed into a box with volume V, coupled to a heat reservoir at temperature T. Then, a partition is introduced in the middle of the box and the demon measures on which side of the partition the molecule is located. The demon then replaces the partition with a piston with some load connected to it. As the gas expands, it performs some work $W = k_B T \ln 2$ on the piston until it

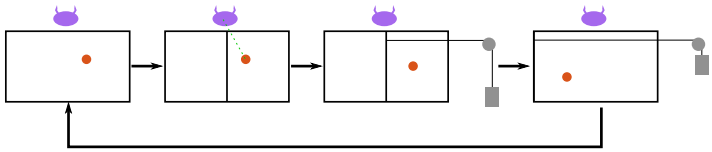

Figure 2.3: Szilard's implementation of Maxwell's demon uses a single particle gas (red dot) in a box. It introduces a partition and measures which side of the partition the particle resides. It then replaces the partition with a piston and allows the gas to expand.

has reached the end of the box after which it is removed. During the expansion, the heat bath supplies the gas with the energy $Q = W$. The system is now reset to its initial stage and the cycle can begin anew. Work has now been extracted from a single heat bath in a cyclical engine, indicating a violation of the Kelvin statement of the second law.

4.3 Landauer erasure and the exorcism of Maxwell's demon

While Szilard understood that memory was important to explain Maxwell's demon, it was not until the work of Landauer its significance was understood. When making the measurement, a bit of information is stored physically in the demon's memory in some way. As work is being extracted, this bit of information is erased from the memory. According to Landauer's principle, such an erasure of memory is necessarily accompanied by dissipation of energy and at least a $k_B \ln 2$ increase of entropy in the environment [20, 21]. Thus, thanks to Landauer's principle, Maxwell's demon is in fact not violating the second law of thermodynamics. Landauer's original proof actually assumed the second law to hold, but the same result has later been derived without such assumptions [54, 55]. $k_B T \ln 2$, the mininum energy dissipated during the memory erasure, is known as the Landauer limit. It is by extension also the bound for how much energy can be extracted from one bit of information in an engine such as Szilard's.

4.4 Generalizing the second law with information

Since the introduction of information and feedback can seemingly violate bounds set by traditional thermodynamics, it was necessary to generalize many of the relations described in the previous sections. For a feedback protocol with a single measurement of the state x, where the applied control parameter λ de-

pends on the measurement outcome y, the information content gained by the measurement is given by

$$I = \ln \frac{P(x,y)}{P(x)P(y)}, \tag{2.21}$$

which averages to the mutual information between x and y over many trajectories. In cases where there are two possible measurement outcomes and no measurement error, $I = \ln 2$, representing one bit of information. Sagawa and Ueda showed that in measurement-feedback scenarios such as these, the Jarzynski equality can be generalized to [22]

$$\left\langle \exp\left(-\frac{W - \Delta F}{k_B T} - I\right)\right\rangle = 1. \tag{2.22}$$

Just like the Jarzynski equality leads to the second law relation of Equation (2.5), Equation (2.22) implies that

$$\langle W \rangle \geq \Delta F - k_B T \langle I \rangle, \tag{2.23}$$

which shows how the inclusion of information weakens the second law for the system. For the Szilard engine in absence of measurement error, $\langle I \rangle = \ln 2$ and $\Delta F = 0$, giving the same bound as Landauer's principle.

Equation (2.23) provides a bound for the maximum work that can be extracted from the information gained in a measurement. There are other ways to quantify the information which also have their own corresponding second law-like inequalities on the form of Equation (2.23) [56].

4.5 Experimental implementations of information thermodynamics

Recently, advances in nanotechnology have allowed for experimental realizations of the concepts described above. Landauer's principle was first verified in 2012 by Bérut et al. [57]. They used a colloidal particle trapped in a double-well potential, with the location of the particle encoding a bit of information. Measuring the dissipated heat when that bit of information is erased, they found it approaches the Landauer limit of $k_B T \ln 2$. Since then, Landauer erasure has been implemented in other colloidal particle setups [58, 59], but also with other platforms like nanomagnetic memory bits [60, 61], superconducting flux logic cells [62] and optomechanical resonators [63].

The first Maxwell's demon-type process was realized by Toyabe et al. in 2010 [25],

by using measurements of a particle's location in a staircase-shaped potential to apply feedback which allowed the particle to climb the staircase and gain more free energy than the work that was done to it. Furthermore, Szilard-type engines that can quantifiably extract work from a single bit of information have been implemented using a single-electron box [27, 64] and a colloidal particle [26]. Other implementations include an autonomous Maxwell's demon, where the demon itself takes the form of an on-chip single-electron box [28] and DNA-pulling experiments [29].

Chapter 3

Systems and methods

In this chapter, the electronic transport properties of quantum dot systems are described. For the work in this thesis, the two main systems used are single quantum dots (SQDs) and serial-coupled double quantum dots (DQDs). The quantum confinement and Coulomb blockade effects are introduced in more detail as well as how they lead to the electronic transport characteristics of those two systems. This is done in the framework of the constant interaction (CI) model [65] and following mainly Refs. [66, 67] in the SQD case and Ref. [68] in the DQD case.

1 Single quantum dots

There are two main effects contributing to the energy spectrum of QDs: the quantum confinement effect and the Coulomb blockade effect. First, the confinement will be briefly considered. In a fully three-dimensional structure, the electrons can be treated as free electrons and interactions with the crystal structure are taken into account by using an effective mass instead of the free electron mass. Here, the possible energies for the electrons take on a continuum structure. However, because of wave-particle duality, there is a wavelength associated with the electrons known as the de Broglie wavelength λ_{dB}. If one of the dimensions of the crystal is shorter than λ_{dB}, the electrons are not free to move in that direction and the energy spectrum is modified [69]. In this way, 2D structures, 1D structures and finally 0D structures (QDs) can be formed depending on in how many dimensions the crystal is smaller than λ_{dB}. In a 0D structure, the energy spectrum is then fully discrete with single-particle energy levels ϵ_i.

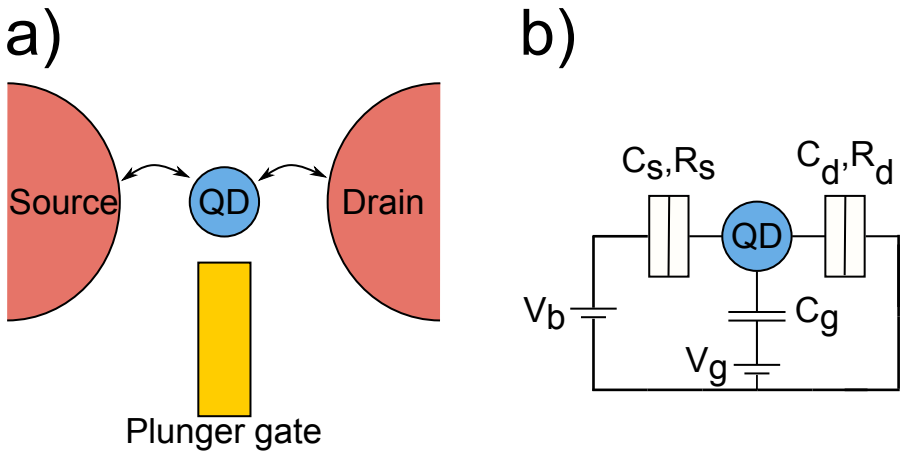

Figure 3.1: a) Schematic of the QD system. One QD is tunnel coupled (illustrated by the arrows) to a source reservoir and a drain reservoir. There is also a plunger gate nearby in order to manipulate the energy levels of the QD. b) Equivalent circuit diagram in the CI model. The tunnel couplings are represented by a capacitance in parallel with a resistance and the QD is capacitively coupled to the gate.

The Coulomb blockade effect can qualitatively be understood as the electrons in the QD repelling other electrons, making them unable to enter. Thus, for more electrons to be added, they need to overcome this electrostatic potential. This effect is present in any small enough conductor and is the foundation for metallic devices such as the single electron box and the single electron transistor. In this section, the CI model [65] will be used to derive the energy needed to add an electron to a QD, following Refs. [66, 67].

A simple SQD system similar to the ones that have been studied experimentally in this thesis is illustrated in Figure 3.1, together with an equivalent circuit diagram. The QD is coupled by tunnel barriers to the source and drain electrodes and capacitively coupled to a gate electrode. The CI model makes two key assumptions. The first is that Coulomb interactions between electrons inside and outside the QD is parametrized only by the QD self-capactitance C_Σ. The second is that the discrete energy levels arising from quantum confinement are independent on the number of electrons on the QD. First, the electrostatic part of the total energy will be derived. For a system of m conductors, the charge on conductor i is given by

$$Q_i = \sum_{j=0}^{m} C_{ij} V_j, \tag{3.1}$$

where C_{ij} is the capacitance between conductors i and j, and V_j is the electrostatic potential of conductor j. Letting the QD have index 0 and noting its

self-capacitance can be written as a a sum of its capacitances to the electrodes $C_\Sigma = C_{00} = \Sigma_{j\neq 0} C_{0j}$, the electrostatic potential of the QD is

$$V_0 = \frac{1}{C_\Sigma}\left(Q_0 - \sum_{j=1}^{m} C_{0j}V_j\right). \tag{3.2}$$

From here, the total electrostatic energy of a QD charged with N electrons is found by integrating V_0 over Q_0 from 0 to $-eN$, where e is the elementary charge, yielding

$$U(N) = \frac{e^2N^2}{2C_\Sigma} + eN\sum_{j=1}^{m}\frac{C_{0j}}{C_\Sigma}V_j. \tag{3.3}$$

The total energy of the QD also includes the single-particle energies ϵ_i that arise from quantum confinement. In the CI model, these are N-independent and can thus be added to the electrostatic energy like so:

$$E(N) = \sum_{i=1}^{N}\epsilon_i + \frac{e^2N^2}{2C_\Sigma} + eN\sum_{j=1}^{m}\frac{C_{0j}}{C_\Sigma}V_j. \tag{3.4}$$

It is now convenient to introduce the lever arm $\alpha_j = -\frac{C_{0j}}{C_\Sigma}$. It is a parameter that is used to translate the voltage applied to a surrounding electrode to a shift in electrochemical potential of the QD. The electrochemical potential $\mu(N)$ is a measure of how large the change of energy is when adding the Nth electron to the QD and is thus given by

$$\mu(N) = E(N) - E(N-1) = \epsilon_N + \frac{e^2}{C_\Sigma}\left(N - \frac{1}{2}\right) - e\sum_{j=1}^{m}\alpha_j V_j. \tag{3.5}$$

This derivation comes to an end with the addition energy, which is the change in μ when the Nth electron is added. That is,

$$E_{add}(N) = \mu(N) - \mu(N-1) = E_\Delta(N) + E_C, \tag{3.6}$$

where E_Δ is the level spacing of the single-particle energies $(\epsilon_N - \epsilon_{N-1})$ and E_C is the charging energy due to Coulomb interactions $(\frac{e^2}{C_\Sigma})$.

The quantized nature of the electrochemical potential in gives rise to the interesting transport properties of QDs. Applying a bias voltage between the source and drain electrodes should allow electrons to move from one to the other via the QD. However, if there is no energy level within the bias window (as in Figure 3.2a) the electron will be prohibited from entering the QD and there will

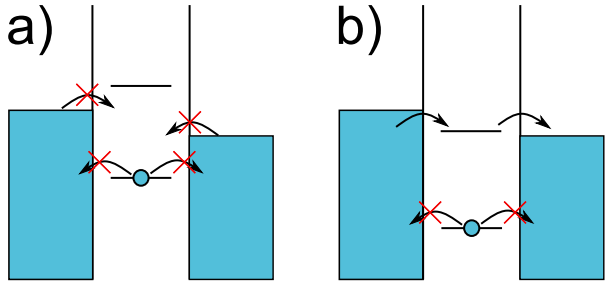

Figure 3.2: Energy diagrams for electron transport through a SQD. In a), there is no QD energy level inside the bias window and transport is blocked. In b), one of the levels has been shifted into the bias window and is now available for transport.

be no transport. This is known as the Coulomb blockade effect. According to equation 3.5, the chemical potential can be shifted by applying a gate voltage. Once an energy level has been shifted into the bias window (as in Figure 3.2b), transport can occur.

It is now important to note the two necessary conditions to observe the well-defined single-electron tunneling. First, the tunnel resistances R_s and R_d must both be larger than the quantum resistance $\frac{h}{e^2}$ where h is Planck's constant. This is because in order for the electron wave function to be localized on the QD, the uncertainty in energy has to be smaller than E_C [65]. The second condition is that the thermal energy k_BT where k_B is Boltzmann's constant and T is the temperature must be smaller than E_C in order to avoid thermal smearing.

If both the bias voltage V_b between source and drain and the gate voltage V_g are swept while monitoring the current I through the device, a charge-stability diagram like the illustration in Figure 3.3 can be constructed. This diagram is a useful tool for characterizing QDs, allowing one to extract parameters such as E_C, E_Δ, C_g and α_g as well as perform excited state spectroscopy.

If the bias voltage is applied symmetrically, the chemical potential of source and drain are given by $\mu_S = \mu_0 + e\frac{V_b}{2}$ and $\mu_D = \mu_0 - e\frac{V_b}{2}$ respectively, where μ_0 is the chemical potential of both source and drain without the applied V_b. This gives the following conditions for the system to be in the Coulomb blockade regime, where an energy level of the QD is not within the bias window:

$$\left.\begin{aligned} \mu_N &< \mu_0 - \frac{eV_b}{2} \\ \mu_{N+1} &> \mu_0 + -\frac{eV_b}{2} \end{aligned}\right\} \text{for } V_b > 0 \text{ and } \left.\begin{aligned} \mu_N &< \mu_0 + \frac{eV_b}{2} \\ \mu_{N+1} &> \mu_0 - \frac{eV_b}{2} \end{aligned}\right\} \text{for} V_b < 0.$$

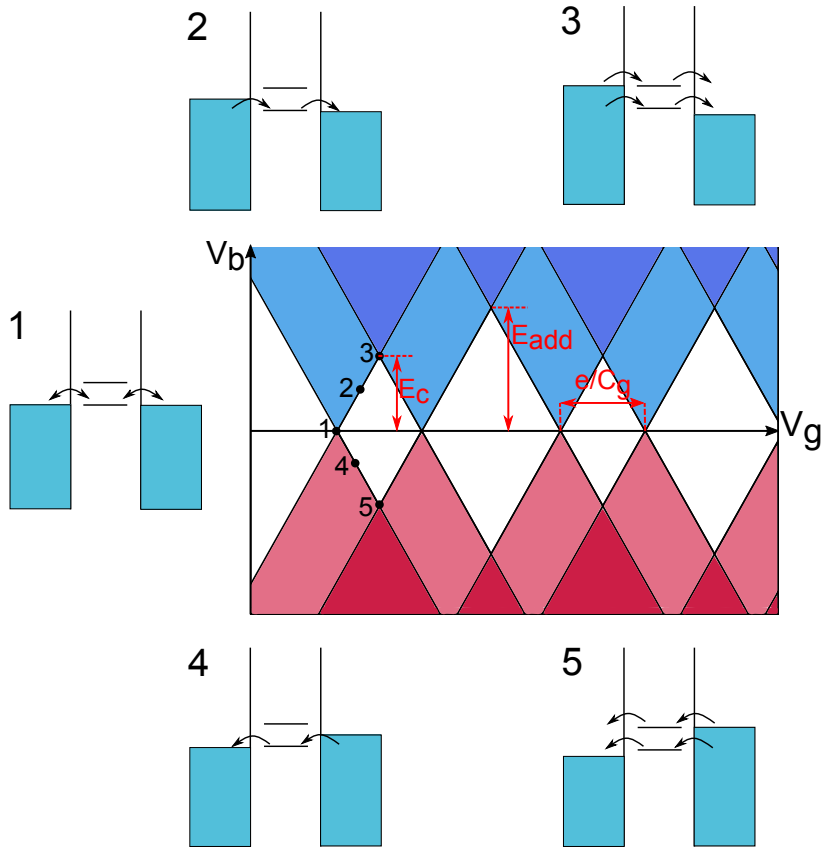

Figure 3.3: Charge stability diagram for a SQD. The white regions indicate that transport is blocked because no energy level is within the bias window. In light areas, one energy level is within the window and in the dark areas the excited state has also entered the window. The difference between blue and red means current flows in opposite directions. Along the edges of the diamonds, one energy level is exactly aligned with either the source or drain edge, which is illustrated in points 1-5.

Taking the edge cases of these inequalities and substituting into equation 3.5 gives the relation between V_b and V_g. In the case $V_b > 0$, it is given by

$$V_g = \frac{1}{e\alpha_g}\left[\epsilon_N + E_C\left(N - \frac{1}{2}\right) - \mu_0 + \frac{eV_b}{2}(1 - \alpha_S + \alpha_D)\right], \tag{3.7}$$

$$V_g = \frac{1}{e\alpha_g}\left[\epsilon_{N+1} + E_C\left(N + \frac{1}{2}\right) - \mu_0 - \frac{eV_b}{2}(1 + \alpha_S - \alpha_D)\right], \tag{3.8}$$

and similar for the $V_b < 0$ case. These lines define the diamond-shaped regions of no current and well-defined charge state in Figure 3.3, known as Coulomb diamonds. The slope of the lines depend on the lever arms for each of the electrodes α_S, α_D and α_G. For simplicity, Figure 3.3 shows the diagram of a QD with symmetric tunnel barriers ($\alpha_S = \alpha_D$). In that case, the slopes are

simply given by $\pm\frac{1}{2e\alpha_g}$. For an asymmetric QD, the Coulomb diamonds would be slanted in some direction depending on which tunnel coupling is stronger. The two lines defined by equations 3.7-3.8 intersect when $V_b = eE_{add}(N+1)$, allowing one to extract the addition energy. Along the V_g-axis, the distance between corners of the Coulomb diamonds is given by $\Delta V_g = \frac{1}{e\alpha_g}E_{add}(N+1)$.

The first large Coulomb blockade region in Figure 3.3 corresponds to when the QD is completely depleted of electrons. The subsequent Coulomb diamonds vary in size because of degenerate energy levels. The Δ_E-term in E_{add} will only contribute when a new energy level ϵ_i starts being filled. In a spin-degenerate system like in Figure 3.3, two electrons will be able to occupy each level so only the charging energy needs to be overcome to add every second electron. The distance between corners along the V_g-axis in a small diamond is $\Delta V_g = \frac{1}{e\alpha_g}E_C = \frac{e}{C_g}$, giving the gate capacitance.

In the light coloured areas, exactly one energy level is within the bias window. The charge state shuffles between N and $N+1$ and a current can run through the device. For sufficiently large biases, more than one energy level can enter the window and a larger current can flow. This is represented by the dark coloured areas in Figure 3.3.

2 Double quantum dots

By introducing a tunnel barrier between two quantum dots each coupled to a reservoir (as illustrated in Figure 3.4a)), a serial-coupled double quantum dot (DQD) is formed. To transport an electron from source to drain, it needs to move between the two QDs. This means there needs to be an energy level from each QD in the bias window, otherwise transport is blocked. Figure 3.4b) shows the equivalent circuit diagram for a typical DQD system. Compared to the SQD case, there are now two gate voltages (to give independent control of each QD) V_{gl} and V_{gr}. These are coupled to the corresponding QD with the capacitances $C_{gl,L}$ and $C_{gr,R}$. However, there will also exist a cross-coupling to the other QD which is represented by the capacitances $C_{gr,L}$ and $C_{gl,R}$. The interdot coupling is represented by the additional capacitance C_m. Because of this coupling capacitance, the charge state of one QD is not independent of the charge state of the other. The following discussion on the electrochemical potential is again based on the constant interaction model and follows Ref. [68]

To start with, the linear transport regime ($V_b = 0$) is considered. In addition,

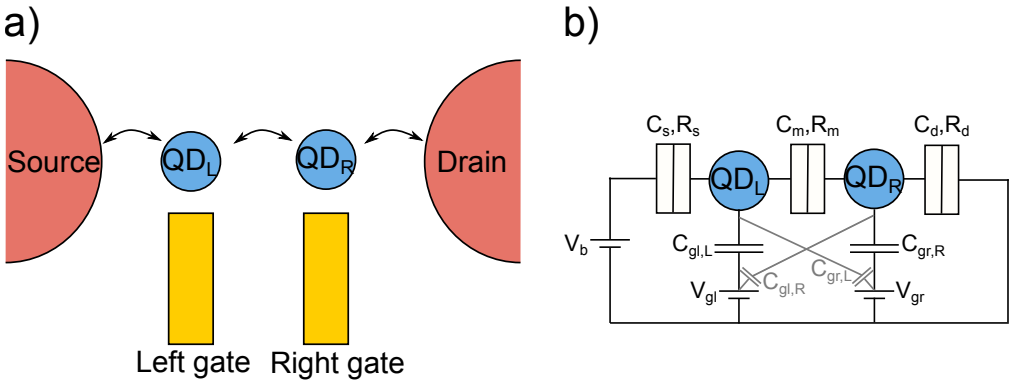

Figure 3.4: a) Schematic of the DQD system. The QDs are coupled in series so that each dot is coupled to one reservoir and to the other dot. Each QD has its own designated plunger gate to manipulate the energy levels. b) Equivalent circuit diagram in the CI model.

the cross-coupling capacitances $C_{gl,R}$ and $C_{gr,L}$ are assumed to be negligible. For simplicity, the gate capacitances $C_{gl,L}$ and $C_{gr,R}$ are from now on referred to as C_{gl} and C_{gr}, respectively. Then, the electrostatic energy of a DQD system with N electrons on the left dot and M on the right dot is given by

$$\begin{aligned} U(N,M) =& \frac{1}{2}N^2E_{C,L} + \frac{1}{2}N^2E_{C,R} + NME_{C,m} + f(V_{gl},V_{gr}), \\ f(V_{gL},V_{gR}) =& \frac{1}{e}\left[C_{gl}V_{gl}(NE_{C,L}+ME_{C,m}) + C_{gr}V_{gr}(NE_{C,m}+ME_{C,R})\right] \\ &+ \frac{1}{e^2}\left[\frac{1}{2}C_{gl}^2V_{gl}^2E_{C,L} + \frac{1}{2}C_{gr}^2V_{gr}^2E_{C,R} + C_{gl}V_{gl}C_{gr}V_{gr}E_{C,m}\right], \end{aligned} \tag{3.9}$$

where $E_{C,L(R)}$ is the charging energy of the left (right) QD and $E_{C,m}$ is the coupling energy, that is the energy change in one QD when an electron is added to the other. In terms of capacitances these are written the same way as SQD charging energies, but with a factor to account for the coupling:

$$E_{C,L(R)} = \frac{e^2}{C_{L(R)}}\left(\frac{1}{1-\frac{C_m^2}{C_{L(R)}C_{R(L)}}}\right), \tag{3.10}$$

$$E_{C,m} = \frac{e^2}{C_m}\left(\frac{1}{\frac{C_LC_R}{C_m^2}-1}\right). \tag{3.11}$$

In equations 3.10-3.11, $C_{L(R)}$ refers to the self-capacitance of the left (right) dot which, again, is the sum of all capacitances to that dot. With two QDs, the chemical potential $\mu_L(N,M)$ is the energy needed to add the Nth to the left QD while the electron number on the right dot stays M and vice versa for

$\mu_R(N, M)$. Adding the single-particle energy levels to the electrostatic energy from equation 3.9 to get the total energy $E(N, M)$ like in Section 1, they are written as

$$\mu_L(N, M) = E(N, M) - E(N-1, M) = \left(N - \frac{1}{2}E_{C,L}\right) + ME_{C,m} - \frac{1}{e}(C_{gl}V_{gl}E_{C,L} + C_{gr}V_{gr}E_{C,m}) + \epsilon_{L,N}, \tag{3.12}$$

$$\mu_R(N, M) = E(N, M) - E(N, M-1) = \left(M - \frac{1}{2}E_{CR}\right) + NE_{Cm} - \frac{1}{e}(C_{gl}V_{gl}E_{C,m} + C_{gr}V_{gr}E_{C,R}) + \epsilon_{R,M}. \tag{3.13}$$

The addition energy is again defined as the change in chemical potential when an electron is added and thus given by

$$E_{add,L} = \mu_L(N+1, M) - \mu_L(N, M) = E_{C,L} + \Delta_{E,L}, \tag{3.14}$$

$$E_{add,R} = \mu_R(N, M+1) - \mu_R(N, M) = E_{C,R} + \Delta_{E,R}. \tag{3.15}$$

Just like outlined in Section 1 for the SQD case, the stability diagram is an important characterization tool for DQDs. However, since there are now three voltages to vary (V_{gl},V_{gr} and V_b), the bias voltage is typically set to a constant value. To start with, the linear response regime is again considered. As long as no energy levels in either QD is aligned with either the chemical potential in the source and drain or in each other, the charge state of the DQD is stable.

The shape of the stable regions in the V_{gl}-V_{gr} plane depends the strength of the coupling between the QDs [68]. Figure 3.5a)-c) illustrate the borders of the charge state for three different cases. In the case where $C_m = 0$ and the two QDs are uncoupled, the stable charge regions are simply square like in Figure 3.5a). Crossing from one square to another means an electron is either added to or removed from one of the QDs. The other limit is shown in Figure 3.5b) and occurs when the coupling capacitance is the dominating term in the self-capacitance sum. Here, the coupling between the two QDs is so strong that the DQD behaves like one QD with charge $N + M$. Sweeping only one of the gate voltages would here simply show the characteristic Coulomb oscillations of a SQD.

Finally, in the intermediate coupling regime, the charge stability diagram becomes a honeycomb lattice like the one in Figure 3.5c). There are lines of three different slopes which each correspond to a different type of charging event,

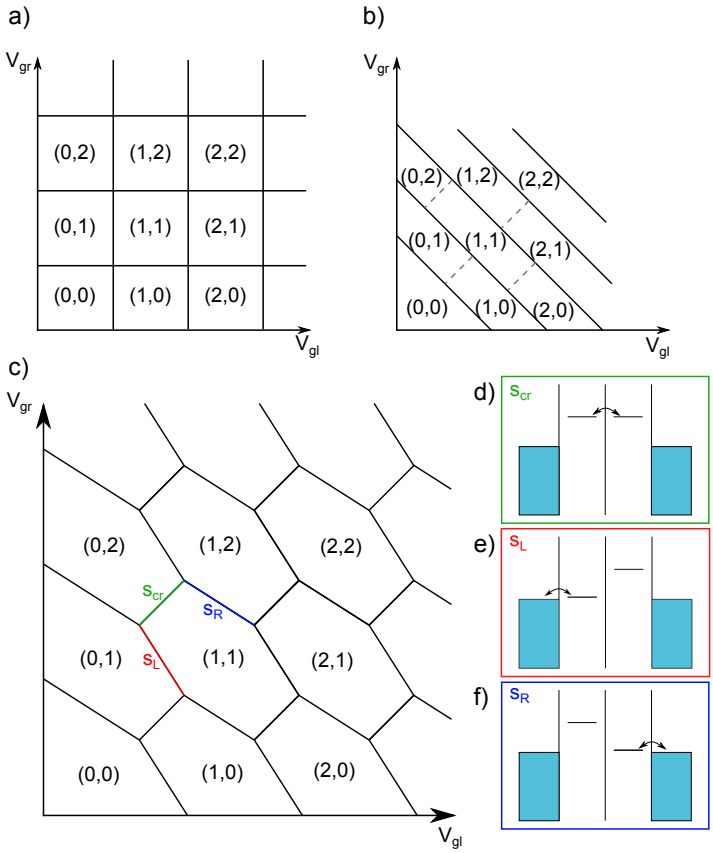

Figure 3.5: Charge stability diagram for a DQD. in three different regimes. In a), there is no interdot coupling and adding a dot to the left dot has no effect on the electrostatics of the right dot and vice versa. In b), the interdot coupling is very strong and the DQD features are entirely lost, the system instead acts a large SQD. In c) there is intermediate coupling and the corners from a) have split into triple points, leading to hexagonal charge states. Three distinct slopes can be seen, corresponding to transition between QDs (d), the left lead (e) and the right lead (f).

as illustrated in Figure 3.5d)-f). Two of the slopes correspond to a charging event involving either the source or the drain, shown in Figure 3.5e)-f). The third slope indicates an electron being transported between the two QDs, see Figure 3.5d). These slopes can be used to extract the lever arms $\alpha_{gl/r,L/r}$ [70] which here is the conversion factor between the gate indicated by lower case and a shift in chemical potential on the QD indicated by upper case. Using the fact that each charging line corresponds to the chemical potential of one QD stays constant, the slopes $s_{L/R} = \frac{dV_{gr}}{dV_{gl}}$ can be determined to be

$$s_{L/R} = -\frac{\alpha_{gl/r,R/L}}{\alpha_{gr/l,L/R}}. \tag{3.16}$$

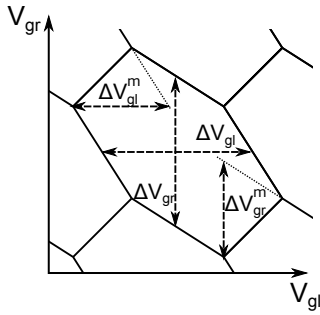

Figure 3.6: Zoomed in honeycomb in charge stability diagram, marking the voltages needed to characterize the DQD.

Likewise, using the fact that along the charge reconfiguration line, both chemical potentials shift an equal amount, the slope of that line is

$$s_m = \frac{\alpha_{gl,L} - \alpha_{gl,R}}{\alpha_{gr,R} - \alpha_{gr,L}}. \tag{3.17}$$

In the corner of each hexagon, the three lines intersect. At these points, called triple points, the chemical potentials throughout the whole system are aligned. The triple points are the only points where an electron can move unobstructed between the two leads.

Figure 3.6 shows a closer look at one honeycomb cell. Much like for a SQD, the dimensions of the blockaded regions can be used to extract important parameters of the DQD. Using the notation from Figure 3.6, the voltage range spanning two charging lines and the separation between charging lines due to the interdot coupling are [68]

$$\Delta V_{gl/r} = \frac{e}{C_{gl/r}} \left(1 + \frac{\Delta_{E,L/R}}{E_{C,L/R}}\right), \tag{3.18}$$

$$\Delta V^m_{gl/r} = \frac{eC_m}{C_{gl/r}C_{R/L}} \left(1 + \frac{\Delta_{E,L/R}}{E_{C,m}}\right), \tag{3.19}$$

respectively.

In order to fully characterize the DQD system, it is not sufficient to study the linear response regime. It is necessary to apply a bias voltage and study the finite bias regime. With a bias window opened, a current can flow through the device if each QD has an energy level in the right configuration within the window. This causes the triple points of the stability diagram to grow into triangular areas, called finite bias triangles, illustrated in Figure 3.7a). The size of the triangles depend on the size of the bias window. If V_b is applied to the source (left) and the drain (right) is kept grounded, i.e. $\mu_S = -eV_b$ and $\mu_D = 0$,

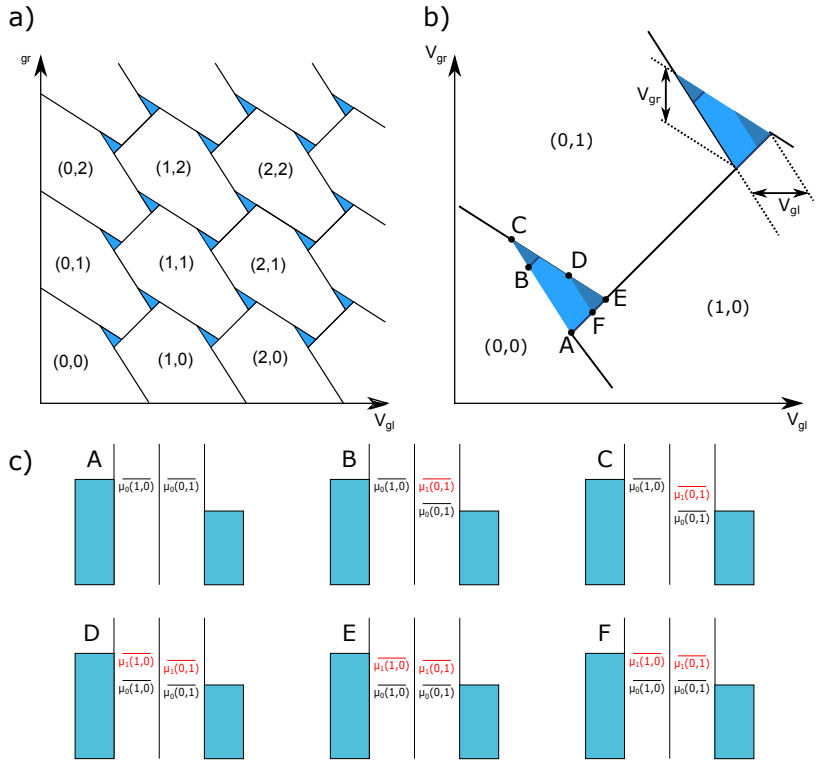

Figure 3.7: a) The charge stability diagram for a DQD with an applied bias. The triple points have expanded to finite bias triangles, where current can flow. b) Closer look at a pair of bias triangles, where features due to excited states are visible. Here, a darker colour means a higher current. c) Energy diagrams corresponding to the letters around the triangle's edges in b). The excited states are shown in red.

the triangles are bounded by $-eV_b \geq \mu_L$, $\mu_L \geq \mu_R$ and $\mu_R \geq 0$. In Figure 3.7b), $\delta V_{gl/r}$ is given by

$$\delta V_{gl/r} = \frac{eV_b}{\alpha_{gl/r,L/R}}, \tag{3.20}$$

allowing for the extraction of lever arms (and thus, capacitances) of the system. Using equations 3.16-3.17, the lever arms between QD and opposite plunger gate voltage can be derived as [70]

$$\alpha_{gl,R} = -s_R \alpha_{gr,R}, \tag{3.21}$$

$$\alpha_{gr,L} = \frac{s_m - s_R}{s_m - s_L} \alpha_{gr,R}. \tag{3.22}$$

Equations 3.20-3.22 together with equations 3.14-3.15 allows for the extraction of all relevant parameters such as addition energies, coupling energy, and gate- and self-capacitances of the QDs.

Again in analogy with the SQD case, the finite bias regime can be used to perform excited state spectroscopy [68, 71]. Within the finite bias triangle, the current is generally not constant, but instead depends on how many excited states are available for transport in the bias window and their alignment. Figure 3.7b)-c) shows a schematic of a pair of bias triangles where one excited state per QD is relevant. The ground states are labeled $\mu_0(1,0)$ and $\mu_0(0,1)$ with excited states $\mu_1(1,0)$ and $\mu_1(0,1)$. The current will always peak when two QD states are exactly aligned, since it allows for elastic electron tunneling. One such peak is found at the bottom of the triangle, along the charge reconfiguration line where the two ground states are always aligned. Starting at the bottom left of the triangle and moving up along the source charging line, $\mu_0(0,1)$ is pulled down and the two states are misaligned. The current decreases, but is not completely suppressed because inelastic tunneling is still allowed. Eventually, the levels have been pulled down enough so that $\mu_1(0,1)$ is aligned with $\mu_0(1,0)$ and another elastic tunneling peak appears. Moving from the peak to the top of the triangle, only inelastic tunneling is possible, but there is now an extra state available for transport so the current is higher than on the other side. When going from the top of the triangle along the drain charging line, eventually $\mu_1(1,0)$ is pulled into the bias window. It is not aligned with any other energy level, so there is no peak but the current is again increased due to a higher number of channels.

Up until this point, only sequential tunneling events have been considered to contribute to transport. That is, events where electrons first enter and then leave the QDs one by one. However, if the tunneling rate is fast enough that the time scale is smaller than the time scale of Heisenberg's uncertainty relation, an electron can move to a virtual, energetically unfavourable, state for this short amount of time. This process is known as cotunneling and allows for transport to occur even when sequential tunneling is suppressed by the Coulomb blockade effect [72–74]. In the DQD charge stability diagram, this shows up as current around the charging lines [75]. Either an electron cotunnels from source to the right QD or from the left QD to the drain.

3 Forming quantum dot systems in nanowires (Paper I)

This chapter introduces ways to practically form quantum dots suitable for performing transport experiments. Both the approaches of forming QDs with electrostatic gating as well as directly with materials are considered and com-

pared before introducing the materials approach specifically used in this work: the polytype-defined QDs. Section 3.3 then describes the experimental work which led to Paper I.

3.1 Gate-defined vs. material-defined quantum dots

The two main approaches for creating confinement in all spatial dimensions and thus forming a quantum dot are electrostatic gating and forming them with materials. In truth, both approaches include materials-engineering, but for simplicity 'material-defined' here means the QDs are fully formed by the materials.

In the gate-defined approach, you start with electrons already confined in at least one dimensions and use gates electrodes to deplete certain regions of electrons. Commonly, the starting point is a two-dimensional electron gas (2DEG) formed at the interface of epitaxially grown semiconductor heterostructures, such as AlGaAs/GaAs [71, 76, 77]. By fabricating electrodes on top, the 2DEG can be shaped into a one-dimensional structure or a QD. More recently, gate-defined QDs using bilayer graphene as the starting point have also been developed [78]. It is also possible to use a one-dimensional structure like a carbon nanotube [79] or a semiconductor nanowire [80] as the starting point. Tunnel barriers are formed in the structure by depleting small sections of the wire of electrons using a nearby gate electrode. The advantage of the gate-defined approach is it allows for very tunable QD systems since each tunnel coupling can be tuned by varying a gate voltage. However, the shape and size of the QDs are susceptible to external noise and not well-defined. In addition, much tuning may be needed to properly form the system.

In a material-defined system, no external gating is required to form the QD. These can further be divided into QDs which require top-down processing to form and QDs that can be formed completely bottom-up. The first type usually involves some form etching. One example is using semiconductor heterostructures to introduce barriers before etching them into mesas to form circular, so called vertical, QDs [81, 82]. Another involves patterning graphene into nanostructures [83, 84]. The bottom-up approach means using growth methods to form the dots. The first examples of this variant used molecular beam epitaxy to form self-assembled dots directly on top of a substrate [85, 86]. Advances in nanowire growth techniques allows for atomically sharp material interfaces in the wires [87]. This enables one to, for example, introduce a short segment of a different material with a higher bandgap to form a tunnel barrier. Introducing several such barriers will form QD systems [88]. The QD systems used in this

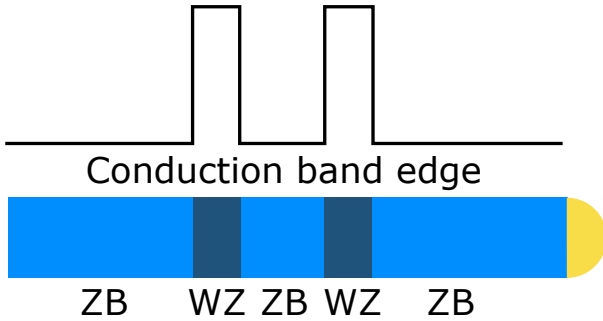

Figure 3.8: Schematic of a polytype-defined quantum dot. The two wurtzite segments introduce a hard barrier for the electrons at the conduction band edge, leading to confinement inbetween them.

work instead introduces a segment with a different crystal structure (but the same material) and is explained in more detail in section 3.2.

3.2 Polytype-defined double quantum dots in InAs nanowires

The double quantum dots used in this thesis were formed in InAs nanowires. InAs has two primary polytypes, defined by how the atomic bilayers stack along the nanowire length [89]. The two polytypes have a relative conduction band offset of around 125 meV, meaning WZ segments would function as tunnel barriers for electrons in the ZB phase as shown in Figure 3.8 [30, 32]. The shallow barrier height means the WZ segments can be made several tens of nanometers long while still allowing tunneling. In a DQD system, this is appealing because the individual QDs can be spaced out more which allows for easier processing of nearby plunger gates as well as smaller cross-capacitances.

The InAs wires here studied were grown using metal organic vapor phase epitaxy (MOVPE). The process uses Au nanoparticles deposited on an InAs substrate to catalyze nanowire growth using trimethyl indium and arsine as precursor gases. By varying the ratio of In precursor to As precursor, the crystal phase of the nanowire can be switched with atomic layer precision during growth [31]. By making the fraction of As precursor smaller, WZ segments are obtained.

Since the polytype structures can be hard to tell apart using simple characterization techniques a shell of GaSb was grown on top of the InAs. Because of differences in surface energy between ZB and WZ, GaSb can be grown selectively only on ZB parts of the nanowire [90]. This meant that the 20nm GaSb shell was not grown on the WZ tunnel barriers, allowing for very easy identification by scanning electron microscopy (SEM). A cross section-sketch of the nanowire

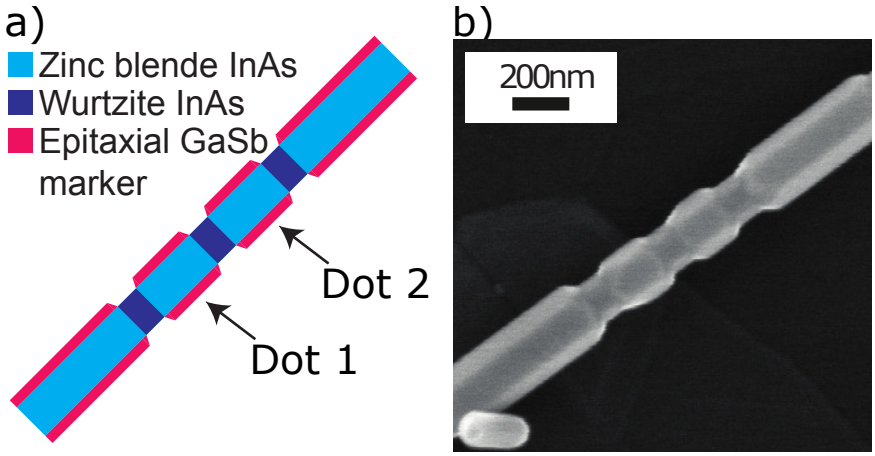

Figure 3.9: a) Cross-section of a polytype-defined DQD, marking the different WZ and ZB sections as well as the GaSb marker layer. b) SEM image of an actual wire deposited to a substrate. The GaSb shell can clearly be seen, indicating where the tunnel barrier are located.

DQD structure as well as one such SEM image is shown in Figure 3.9 [91].

3.3 Polytype-defined double quantum dots: transport experiments

In order to characterize the DQD, transport experiments need to be performed [91]. To do that, lead electrodes and gate electrodes needed to manipulate the electronic states in the device were fabricated. First, nanowires were transferred from the growth substrate to a Si chip and a suitable nanowire was found using SEM. Then, the electron beam lithography (EBL) resist PMMA 950 A5 was spincoated over the entire chip. Next, the shape and position of the electrodes were defined using EBL. The sections of PMMA hit with the electron beam are broken down into smaller polymers which can be dissolved by a developer. Before the actual metal for the electrodes could be deposited, three steps were taken: the GaSb shell was etched away using MF-319 developer, resist residue was removed by oxygen plasma ashing, and the wire's native oxide was etched with buffered oxide etchant. One 25 nm layer of Ni to improve the contact quality and one 75 nm layer of Au were deposited using metal evaporation. Finally, the PMMA was dissolved in acetone, lifting off any metal deposited on top. The GaSb etch step could also be done as the very last step. Figure 3.10 shows an SEM image of the final device before (Figure 3.10a)) and after (Figure 3.10b)) the GaSb shell was removed, illustrating how well-aligned the plunger gates (PG1 and PG2) are to the two QDs.

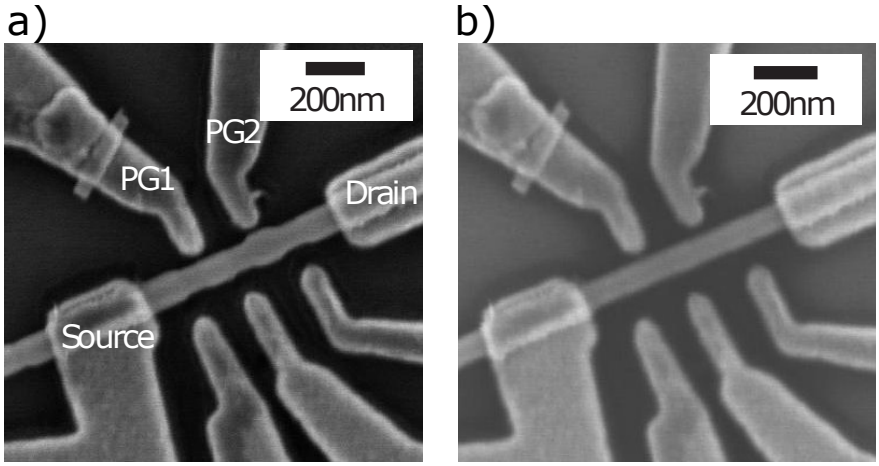

Figure 3.10: SEM images of a DQD device before (a)) and after (b)) etching of the GaSb shell. Both gate and contact electrodes have been patterned with high precision.

The transport measurements were performed in a dilution refrigerator at an electronic temperature of ∼50mK in order to prevent thermal smearing of the Coulomb blockade. Applying a 1 mV bias voltage and sweeping the voltage of PG1 and PG2 reveals a charge-stability diagram showing most of the features discussed in Section 2, see Figure 3.11. The honeycomb lattice of charge states are clearly visible, marked by the finite bias triangles. Inside the triangles, the excited states can be identified by looking at variations in the current. In the case studied in Figure 3.11, the level spacings were determined to be 400 μeV and 80 μeV.

In this device, the tunnel couplings and electron number can not be tuned independently of one another. Figure 3.12a)-b) show the charge stability diagram for higher plunger gate voltages, i.e. the QDs are filled with more electrons. In Figure 3.12, the honeycomb structure is still clearly visible, but the current through the device is higher. Also, the current appears along the charging lines, which is a sign of cotunneling occuring. Both of these features indicate an increased tunnel coupling. In Figure 3.12b), the tunnel coupling is sufficiently strong that the charge stability diagram looks closer to the SQD case, as was described in Section 2. The tunnel coupling increasing can be attributed to two factors. First, as higher energy states are occupied, the effective tunnel barrier height (from energy level to top of barrier) is decreased. In addition, the wave functions of the high energy electrons will penetrate further into the barrier, decreasing the effective barrier width. In principle, additional gates like the three seen on the opposite site of the plunger gates in Figure 3.10 can be used to tune the tunnel barrier. However, for QDs of this size ($<$ 100 nm in length),

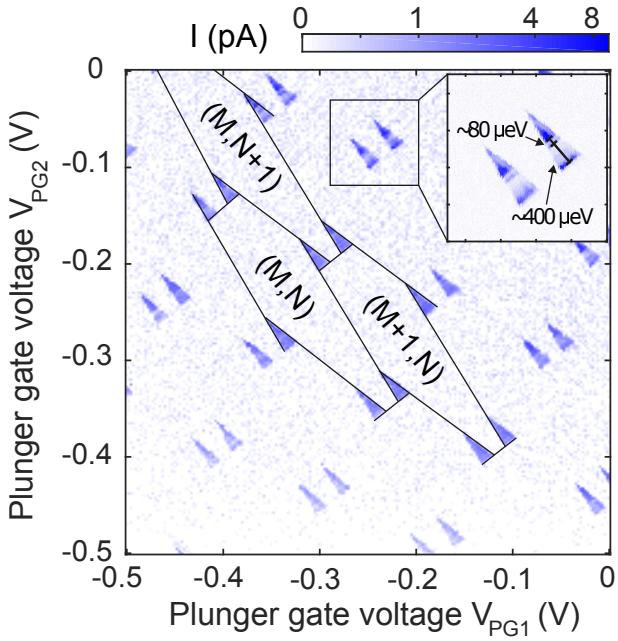

Figure 3.11: Experimentally determined charge stability diagram for a polytype-defined DQD. N and M are electron numbers. Inset: Measurement around a pair of finite bias triangles, showing features arising from excited states.

the cross-capacitive coupling to the dots is large enough that trying to do so will also significantly effect the electron number.

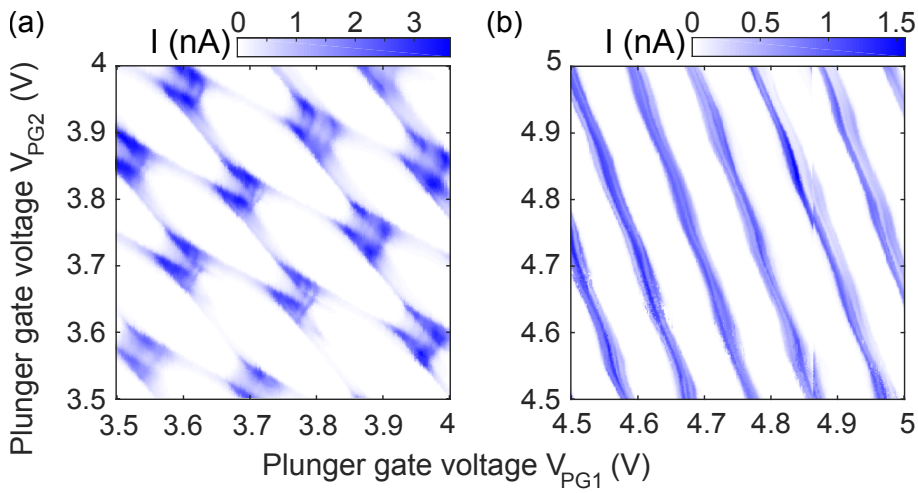

Figure 3.12: Experimentally determined charge stability diagrams for increasingly high electron numbers. In a), the DQD structure is still clearly visible but with cotunneling lines. In b), the DQD structure is starting to collapse and approach more of a SQD structure.

4 Charge detection and counting experiments

This section introduces the charge detection technique, which is used to measure changes in the charge state of quantum dots in real time. This allows for the study of the tunnelling of individual electrons, which is a necessary tool for the studying the thermodynamics of single particles. The chapter begins with an overview of different charge detection techniques and their potential, and then introduces in more detail the charge detection scheme used in this work.

4.1 Charge sensing: an overview

Changes in the charge state of a quantum dot was first measured in the early 1990s [92, 93]. A system whose conductance is very sensitive to variations in the electrostatic environment, such as a quantum point contact (QPC) was coupled capacitively to a QD which could be controlled by a gate voltage. When the gate voltage was varied, the Coulomb peaks in the QD were accompanied by a sharp change in the detector QPC conductance. Since passing a Coulomb peak means an additional electron is now loaded into the QD, measuring the current through the detector gives a measure of the charge state. The QPC technique is still widely used for charge detection in top-gate defined QD systems because it is easy to integrate, requiring just one extra gate to be fabricated [94]. Commonly, single-electron transistors (SETs) [95] or another QD [96] are also used as the detector. Then, the very steep change in conductance in the Coulomb oscillations are used as the operation point.

One of the most powerful features of charge sensing is the ability to witness individual tunneling events in real time [97]. If the measurement bandwidth is sufficiently large, so that measurement of the charge detector current is faster than the rate of charging events in the QD, each individual charging event will be seen as an abrupt change in the detector current as opposed to the time-averaged measurement described above. This technique opens up the door for feedback schemes [27], probing of electron tunneling rates [98] and single-shot spin readout, among others [94].

4.2 Integrated DQD system and sensor and tunnel rate measurement

In this work, a DQD system with a third sensor QD all contained within the same InAs nanowire is studied. The nanowire is grown in the same way de-

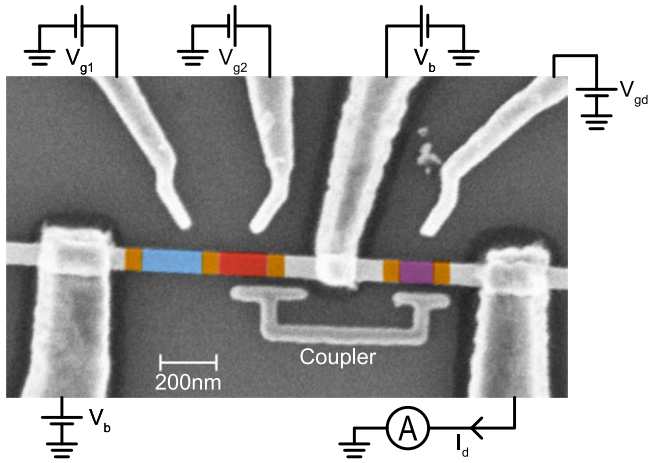

Figure 3.13: SEM image of the type of device used for experiments involving charge detection. The voltages V_{g1}, V_{g2} and V_{gd} each control one QD. By measuring the current through the detector QD I_d, the charge state of the DQD can be read out.

scribed in Section 3.2 and a final device is shown in Figure 3.13. There are now three contact electrodes: one for the DQD, one for the sensor QD, and one common to both. Each QD has its own plunger gate to control their energy levels, labeled V_{g1}, V_{g2} and V_{gd}. In order to increase the coupling between DQD and sensor, a metallic strip is fabricated between them. The coupler is coupled asymmetrically to the DQD in order to differentiate between charging events on the left dot and the right dot.

To demonstrate first the time-averaged charge detection, a 1.5 mV bias voltage is applied across the detector QD. The two contacts of the DQD are made sure to be held at the same potential. Figure 3.14a) shows a sweep of V_{gd}, revealing a Coulomb peak. Because of cross-coupling, changing V_{gd} may effect the charge state of the DQD, which can be seen as the jump in current in Figure 3.14. Likewise, sweeping $V_{g1/g2}$ can influence the setpoint of the detector. For this reason, when applying $V_{g1/g2}$, V_{gd} is also shifted by some compensation factor in order to make sure it stays in the sensitive region over the entire measurement range. Figure 3.14b) shows the DQD charge stability diagram, measured with the charge detector current. The characteristic honeycomb structure is marked by a sudden change in the current, allowing the features to be seen even with no DQD bias applied.

By going to low electron numbers, the tunneling rates can be slowed down enough to be detected in real time. Then, with no bias voltage, the random (thermal) fluctuations of charge can be measured. Tuning the system to stay

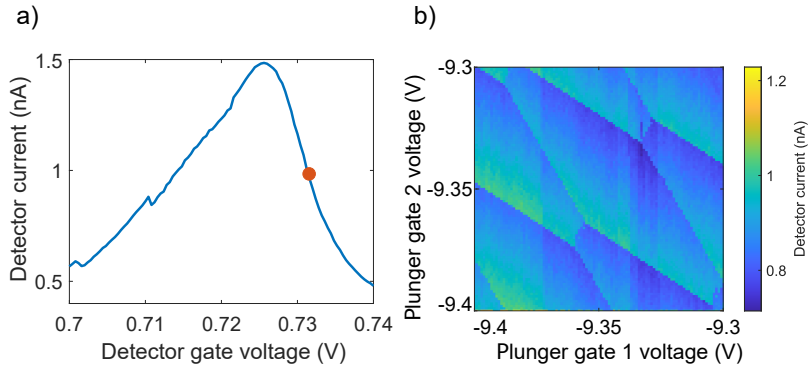

Figure 3.14: a) Sweeping the detector gate voltage shows a Coulomb peak in the detector current. The red dot indicates the most gate-sensitive point which was chosen as the setpoint for detection. b) Monitoring the the detector current while sweeping the DQD gates measures the charge stability diagram, where regions of different charge is bounded by sharp jumps in current.

along one of the charging lines means one of the QDs can exchange electrons with one of the leads, but changes in the other QD are inaccessible. Here, there is an equal chance of having an excess electron either in or out of the QD. Figure 3.15 shows a time trace of the detector current at one such point. Here, the two different charge states are clearly differentiable by the step in current. Because of how the detector's operation point was chosen, the higher current indicates the excess electron is in the QD.

The tunnel-in rate Γ_{in} and tunnel-out rate Γ_{out} can be determined from the waiting times τ_{in} and τ_{out} indicated in Figure 3.15. The tunnel events are independent and follow a Poissonian distribution [99], therefore the waiting times are exponentially distributed:

$$P(\tau_{in/out}) = \Gamma_{in/out} e^{-\tau_{in/out}\Gamma_{in/out}}, \tag{3.23}$$

where $P(\tau_{in/out})$ is the relative probability of observing a waiting time $\tau_{in/out}$. Consequently, the rates can simply be estimated as the inverse mean of the waiting times, provided the measurement time is sufficiently long compared to the waiting times. When moving the DQD energy level away from the chemical potential in the lead, one of the tunnel rates will increase while the other will drop to almost zero. In order to see enough tunneling events in this regime, the measurement time then needs to be increased. In order to avoid this restriction, a feedback scheme [17], described in Figure 3.16a) is used.

An Arduino DUE microcontroller is added to the setup. It monitors the detector current and determines whether it is above or below a certain threshold. Depending on what the Arduino measures, it can use its built-in digital-to-

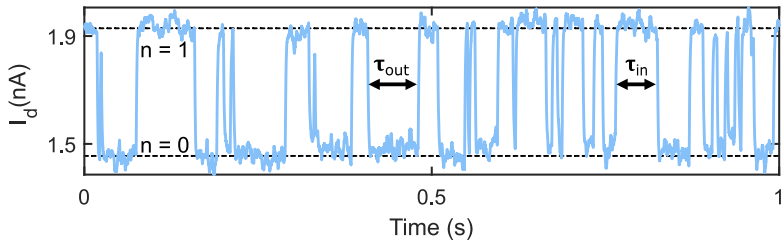

Figure 3.15: Example trace where there is equal probability to find the electron in (high current) or out (low current). The waiting times $\tau_{in/out}$ are indicated as the time spent in one state before the next tunneling event.

analog converter to either add a positive or negative feedback voltage to the DQD plunger gate voltage. If the original setpoint, where there is an equal chance of finding the electron in or out, is called E_0, then the new energy level is $E_0 + \alpha V_{+/-}$ where the subscript indicates the sign of the feedback voltage and α is the conversion factor between voltage and energy. To measure Γ_{in}, initially V_- is applied to make sure an electron on the QD tunnels out. Once it tunnels out, the feedback voltage is swiftly switched to V_+. As soon as an electron tunnels back in, the feedback is once again flipped to V_-. This cycle of preparing an empty state for an electron to tunnel into at V_+ is repeated for the entire measurement duration. By varying the amplitude of V_+, Γ_{in} can be determined over the entire energy range $E_0 - \alpha V_+$ to $E_0 \alpha V_+$. The opposite scheme can be performed to determine Γ_{out}. Both rates as a function of energy for an example charge transition is shown in Figure 3.16b).

In Figure 3.16b), the saturated value for Γ_{out} is roughly twice the saturated value of Γ_{in}. This indicates that the energy level is two-fold spin degenerate and initially half-filled. When tunneling in, only an electron with the opposite spin is allowed to enter the dot. When an electron later tunnels out, either of the two electrons occupying the energy level can exit. If instead the level was initially empty, the relationship between Γ_{in} and Γ_{out} would be reversed. Since the degeneracy clearly influences the tunnelling dynamics, understanding the degeneracy of the system is necessary for most experiments.

4.3 Detector back-action

Before moving on to the information thermodynamics experiments, it is important to consider one potential limitation of the charge detection measurements, namely detector back-action. Back-action is the effect the measurement has on the system itself. A single electron in a quantum dot is a very sensitive sys-

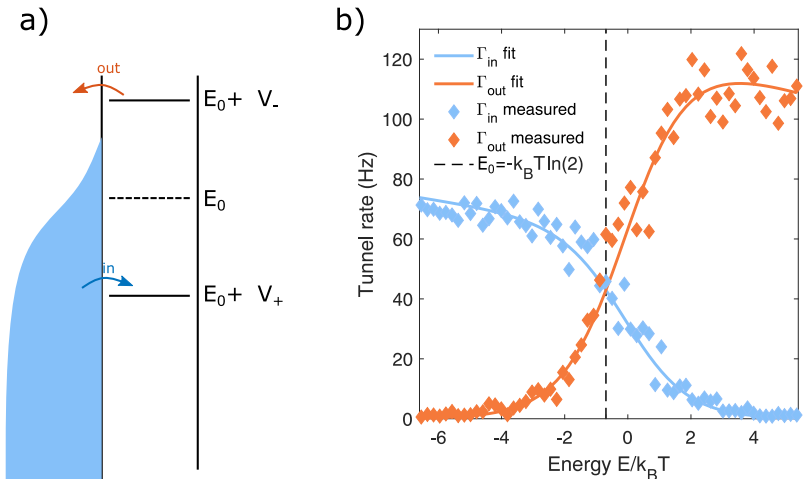

Figure 3.16: a) Illustration of the measurement scheme to determine tunneling rates. Empty or filled states are prepared by driving the level between two points a certain distance away from the energy at which there is an equal probability of finding the electron either in our out once there is a tunneling event. b) Measured tunnel-in rate and tunnel-out rate for a range of energies. Because of two-fold spin degeneracy, Γ_{out} reaches about twice the value of Γ_{in}. The rates are fitted to be proportional to a Fermi function with a superimposed linear dependence to account for the gate voltage affecting the tunnel coupling.

tem, and too much back-action would be detrimental to any experiments. It is important to both understand its mechanisms as well as suppressing its effects. For that reason, back-action has been studied in a variety of detector types including quantum point contacts [100, 101], single electron transistors [102], and graphene nanoribbons [103]. Back-action is a complex process that may arise in several different ways. Three different mechanisms in particular were identified as possible causes of back-action in the system used in the thesis. They are sketched in Figure 3.17.

The first mechanism is called photon-assisted tunneling (PAT) [104–106] shown in Figure 3.17a), which comes about when the energy dissipated in the detector generates photons (or possibly phonons) that lead to inelastic tunneling in the QD under study. Running a current through the detector means the occupation of the detector QD will rapidly fluctuate. Due to the capacitive coupling between detector and the studied QD, these fluctuations effectively modulate the studied QD's energy levels by a time-dependent electric field with frequency f. Then, electrons can exchange photons of energy hf with this external field, where h is Planck's constant, leading to tunnel events that would otherwise be energetically forbidden to occur.

The second mechanism is illustrated in Figure 3.17b), and is also due to the capacitive coupling between the two QDs. Instead of considering the high-

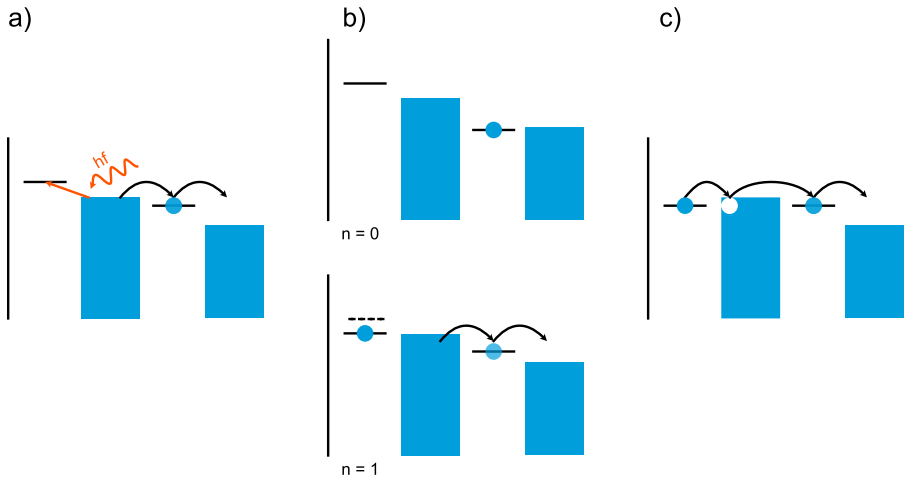

Figure 3.17: Sketches of three potential back-action mechanisms. The blue bars indicate the Fermi energy of the leads, while horizontal lines are discrete energy levels inside the QDs. For simplicity's sake, only the detector QD and QD2 are sketched here. a) Photon assisted tunneling. The power dissipated in the detector generates a photon which excites an electron to the QD. b) Gating of the QD by the detector. In this example, the $n = 0$ state (top panel) on QD2 corresponds to a blockaded state in the detector and no current can run through it. When an electron enters the QD (bottom panel), the current starts running and the average occupation of the detector is lower. This is turn gates QD2, which changes the energy. The dashed line indicates the corresponding energy level from the top panel. c) Charge carrier injection into QD2. In this case, the current generates holes in the QDs' shared lead which can then be injected into QD2, leading to a tunneling-out event.

frequency shaking of energy levels, one can consider the average detector occupation $\langle n_{det} \rangle$. The magnitude of $\langle n_{det} \rangle$ is related to how much the energy levels of the measured QD are effectively gated by the detector. Naturally, since measuring a tunneling event requires a change in the detector current, it also requires a change in $\langle n_{det} \rangle$. If this change is large, it means that every tunneling event in the QD also comes with a significant change in energy. This can be seen in Figure 3.18, which shows the tunneling rates for a QD1 transition measured using the feedback scheme outlined in section 4.2. Here, the detector is operated in a regime such as the one in Figure 3.19, where the bias voltage is small enough that the $n = 0$ state puts the detector QD close to Coulomb blockade and $\langle n_{det} \rangle \approx 0$, whereas the $n = 1$ state puts the detector close to its current peak where $\langle n_{det} \rangle \approx -0.5$. Marking the Fermi energy for the two tunneling rates (i.e. where they reach half of their saturated value) in Figure 3.18 makes it clear that the two rates are shifted in energy, as the they do not coincide. This shift of more than $k_B T$ is attributed to the mismatch in gating between the two states of the detector. In contrast, the tunnel rates previously shown in Figure 3.16 were measured with a detector setpoint such that both states were represented by a current relatively close to the middle of a Coulomb peak where the relative change in $\langle n_{det} \rangle$ is smaller and subsequently the shift was suppressed.

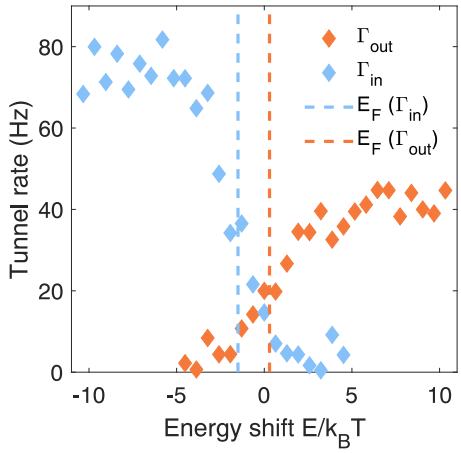

Figure 3.18: Tunnel rates for a QD1 charge transition at 100 mK measured using the same protocol as Figure 3.16, but using a low detector bias such that there is a large change in the average detector occupation when a tunneling event occurs. This leads to the apparent shift in energy between the tunneling rates, here indicated by the separation of their Fermi energies (dashed lines) by $1.6k_BT$.

Finally, the third source of back-action identified is the direct injection of charge carriers into QD2 from its shared lead with the detector QD, as sketched in Figure 3.17c). Ballistic transport has been demonstrated in InAs nanowires over several hundred nm [107], which is on the same order of the distance between those two QDs. That makes the possibility of charge carrier injection a clear concern when studying transitions involving QD2.

In order to determine the device's suitability for experiments on information thermodynamics, measurements of back-action effects were carried out. The three main questions to be addressed by these measurements were: is there any noticeable back-action, is the back-action different for the two QDs of the DQD, and can the effects of back-action be minimized? Since back-action would affect the tunneling characteristics of the systems, the simplest way to investigate it is to measure the tunneling rates using various setpoints on the detector. Note that for these measurements, the main goal was to spot tunneling events occur where they would not be energetically likely without back-action. For this reason, the measurements were carried out at base temperature (to minimize thermally driven events) and without the feedback scheme described in the previous section (since the point of that scheme was to provide better statistics in the regimes of saturated tunnel rates, where back-action will in any case not be as noticeable). Finally, in contrast to Figure 3.13, the two leftmost leads were grounded with the current measured through the middle lead and the bias

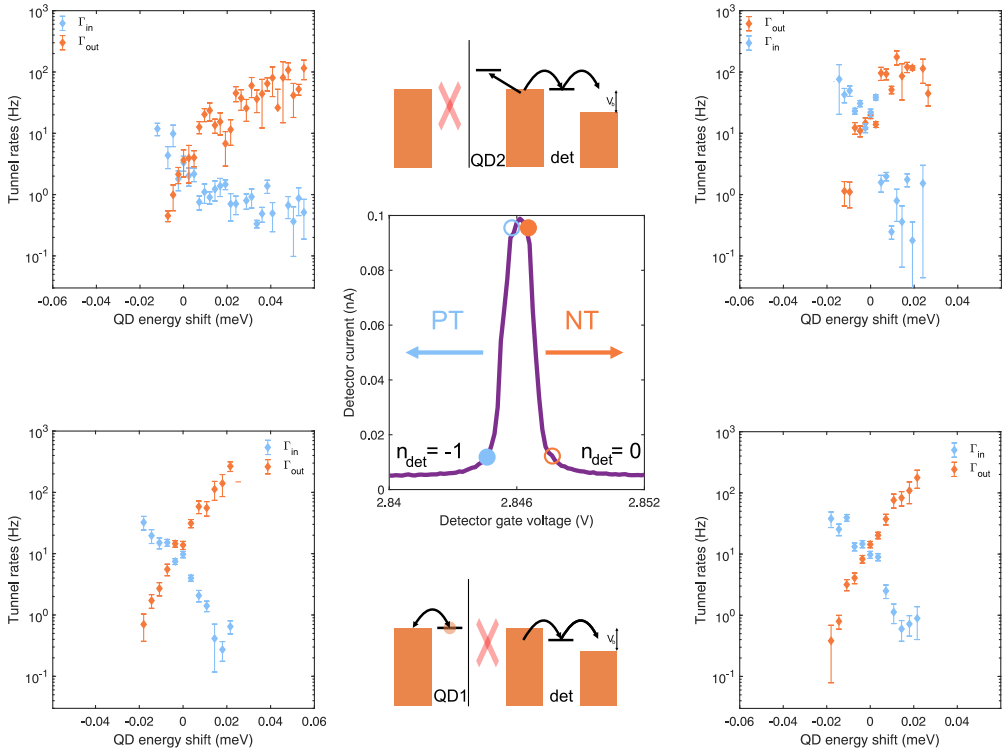

Figure 3.19: The middle panel shows the low-bias Coulomb peak used for charge detection. The orange and blue circles show possible detector setpoints. Here, the circles with same colour represent the $n = 0$ (empty circles) and $n = 1$ (filled circles) for the given setpoint. The panels to the left show tunnel rates measured using the detector set to a region with positive transconductance. In the right panels, they are instead measured with a negative transconductance setpoint. The top corner panels show tunnel rates for a charge transition involving QD2, with an energy diagram sketched in the top middle panel. The red X indicates that QD1 is in Coulomb blockade during the measurement. Also marked is an electron tunneling event which corresponds to the long tail in Γ_{in} from the top left panel. Finally, the bottom panels show the corresponding measurements for a QD1 charge transition.

applied to the rightmost lead.

First, QD2 (the closest one to the detector) was investigated at low ($V_b = 0.15$ mV) detector bias. Two different setpoints in the same Coulomb peak were used. The first is on the left side of the peak where there is a positive transconductance (PT). In this case, the $n = 0$ state in QD2 corresponds to a high detector current. The second setpoint was on the opposite side, with a negative transconductance (NT) and where a high current indicates that QD2 is in the $n = 1$ state. The top corner panels in Figure 3.19 show the measured tunnel rates in this regime. A logarithmic y-axis is used to highlight the small tunneling rates where the effects of back-action should be most noticeable. The most obvious feature here is the long tail in Γ_{in} going to a few Hz in the PT case. Such

a feature does not appear in the corresponding QD1 measurement (bottom left panel), indicating that it may arise from QD2's shared lead with the detector. However, it is not fully consistent with the charge carrier injection picture, since in this particular configuration, the electrons hop away from QD2 as they move through the detector QD and you would then not expect an increase in Γ_{in} for high energies. It is possible that this tail arises from PAT, which would explain why there is no tail in Γ_{out} (since the current generating the photons is turned off while the system is in the $n = 1$ state). However, that does not explain the lack of a corresponding tail in Γ_{out} at the PT setpoint (upper right panel). Clearly, the exact mechanism of this back-action effect is not trivial, and further measurements may be needed to fully understand it.

That same tail is not measured for any setpoint when studying QD1, which is further away from the detector, as seen in the bottom panels of Figure 3.19. This is also consistent with the feedback measurement from Figure 3.18. It appears that for QD1, the gating back-action mechanism is the main potential issue. While it is difficult to estimate the size of the shift from the measurements presented in Figure 3.19 due to the limited statistics for the saturated rates, one can still see that the effect is there when studying the crossover rate where $\Gamma_{in} = \Gamma_{out}$. Depending on if the NT or PT setpoint is used, the crossover rate is different which strongly indicates that the rates are again shifted in energy and that the shift depends on which QD state corresponds to a higher $\langle n_{det} \rangle$. Furthermore, Figure 3.20a) shows that at elevated temperatures the relative difference between the cross-over rate is decreased, indicating that the effect is suppressed. As hinted earlier, the effect can be further suppressed by increasing the bias of the detector to get less of a relative difference in $\langle n_{det} \rangle$. This is also supported by the data in Figure 3.20b) which shows the same type of measurement as in Figure 3.20a) (albeit for a different charge transition), but at $V_b = 1$ mV with the Coulomb peak shown in Figure 3.20c). Here, there is no clear temperature dependence which indicates that the shift is already sufficiently small even at low temperatures. Also, there is no clear contrast between the NT and PT setpoints which is expected if $\langle n_{det} \rangle$ is close to constant in the two cases.

Finally, in order to verify that the back-action effects can be minimized at elevated temperatures, it is important that the temperature of the electronic reservoir follows the bath temperature (set by the cryostat temperature T_{cryo}). In that case, the energy gained during tunneling events arises from thermal excitations rather than from the energy dissipated during detector operation. To measure the electronic temperature T_e, it is first noted that the tunnel rates follow a detailed balance condition $\Gamma_{in}/\Gamma_{out} = \exp(-E/k_B T_e)$ as verfied in Figure 3.20d). By fitting the logarithm of the rates' ratio, it is possible to extract

T_e, which was done for various cryostat temperatures between the base temperature and 150 mK, shown in Figure 3.20e). The saturation noticeable at around 50 mK is the typical electronic temperature saturation in this cryostat. Above that, the electronic temperature closesly follows the cryostat temperature, indicating that the tunneling rates are indeed dominated by the bath temperature. In conclusion, it is possible to to avoid the effects of detector back-action if charge transitions on QD1 are studied, with a high enough detector bias at elevated cryostat temperatures. These conditions are all fulfilled in the rest of the work presented in Chapter 4.

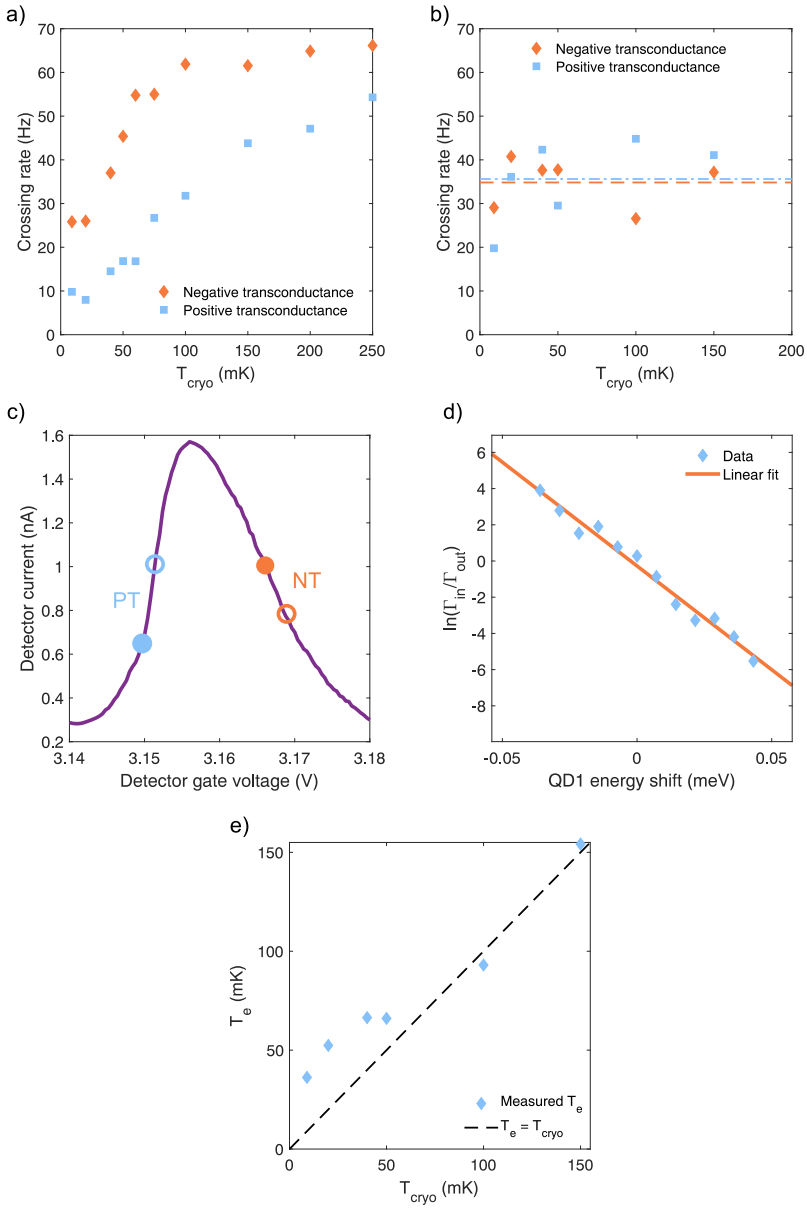

Figure 3.20: a) The tunnel rate at which $\Gamma_{in} = \Gamma_{out}$ for a QD1 charge transition plotted against the cryostat temperature for $V_b = 0.15$ mV and for both a negative transconductance setpoint (orange diamonds) and a positive transconductance setpoint (blue squares). b) The same measurement as in a), but for $V_b = 1$ mV. Note that a different charge transition was used. The dashed lines corresponds to the average crossing rate for the negative transconductance setpoint (orange) and the positive transconductance setpoint (blue). c) The Coulomb peak ($V_b = 1$ mV) used for the measurements in b) and onwards. The circles indicate the current level that at the $n = 0$ (empty) and $n = 1$ (filled) states. d) The logarithm of the ratio of the rates at 100 mK for the negative transconductance setpoint has a linear dependence on energy, as expected for a system that follows detailed balance. e) The electronic temperature T_e extracted from the detailed balance condition with $V_b = 1$ mV. The dashed line indicates when the electronic temperature is equal to the cryostat temperature.

Chapter 4

Information Thermodynamics with Quantum Dots

This chapter presents the bulk of results in this thesis and functions as a summary of Papers II-IV. Since the papers all use the same device and similar measurements, the chapter begins by explaining how to define thermodynamic quantities on the trajectory level for the specific system used in the thesis. Then, an explanation of how to operate the device as a Szilard engine is given. Finally, Papers II-IV are summarized.

1 Thermodynamic quantities

This section serves to connect back to the thermodynamic quantities introduced in Chapter 2. This builds on work done in the group of Jukka Pekola [14, 15, 27], which also used an electronic (but in their case, metallic) system. As a reminder, the device contains three quantum dots and is shown in Figure 4.1a). By placing the middle quantum dot in Coulomb blockade, the very basic system sketched in Figure 4.1b) is obtained experimentally. It is simply one electronic energy level coupled to a Fermionic reservoir. In all papers, this system is operated around a point where one extra electron can enter or leave the energy level. Thus, the system has two possible states: $n = 0$, or $n = 1$. In addition, the energy of these two states are $U_n = nE$ where E is the energy of the electronic level measured from the reservoir Fermi energy. This energy can be driven by a time-dependent gate voltage $\Delta V_1(t)$ (the difference in voltage from the starting point) which acts as the *control parameter*. Then, $E(t) = E_i - \alpha \Delta V_1(t)$, with α

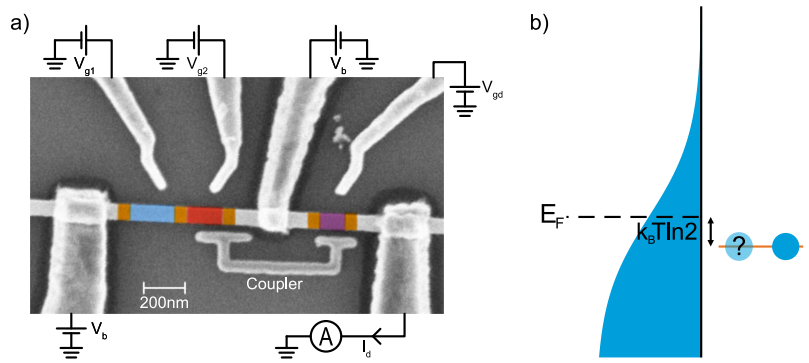

Figure 4.1: a) SEM image of the device used in Papers II-IV. There are three quantum dots (QD1 coloured in blue, QD2 coloured in red and the detector QD coloured in purple). Each QD has a dedicated plunger gate voltage and a bias is applied to run a current through the detector. b) Sketch of the system as the device is operated. A spin-degenerate energy level in QD1 is coupled to a thermal reservoir with Fermi energy E_F. Initially the system is set so that there is an equal chance of an extra electron being on the QD, which occurs when the energy level is offset from E_F by $k_B T \ln 2$.

the lever arm as outlined in Chapter 3 and E_i the energy at the starting point.

1.1 Work and heat

A *trajectory* is fully described by the time evolution of $n(t)$ (which is monitored by the charge detector) and $E(t)$ (which is known from the applied gate voltage). An example trajectory for a process where the energy level is quickly raised before slowly being lowered is shown in Figure 4.2. All relevant thermodynamic quantities can be determined from studying those two. For a trajectory between times $t = 0$ and $t = \tau$, the energy difference is simply $\Delta U = (n(\tau) - n(0))E_0$. In general, what's been of interest for this thesis is how much work W_{ex} is *extracted* from the system and how much heat Q_r is deposited in the reservoir. Since no work is done when moving an unoccupied energy level, W_{ex} is determined by summing up the change in E while $n = 1$, or on integral form:

$$W_{ex} = -\int_0^\tau n(t)\dot{E}_{\text{lev}}(t). \tag{4.1}$$

The third panel of Figure 4.2 shows how the work is accumulated during the duration of the trajectory. Whenever an electron tunnels into the reservoir (i.e. when the system state goes from $n = 1$ to $n = 0$), E worth of heat is deposited. The total heat Q_r for the trajectory is obtained by summing over all the individual jumps, or similarly to equation 4.1:

$$Q_r = -\int_0^\tau \dot{n}(t)E(t)\mathrm{d}t, \tag{4.2}$$

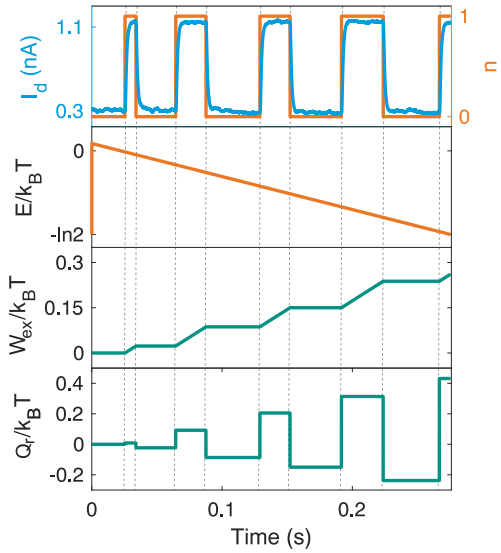

Figure 4.2: A trajectory is defined by the time evolution of $n(t)$ (top panel) and $E(t)$ (second panel). The third and fourth panel shows how extracted work and heat deposited to the reservoir accumulates during the trajectory.

which is shown for the example trajectory in the bottom panel of Figure 4.2.

1.2 The effect of spin degeneracy

Before moving on to how the entropy production over a trajectory is determined, it is instructive to first consider the probabilities p_1 and $p_0 = 1 - p_1$ as functions of energy. For a non-degenerate energy level, $p_1(E)$ would simply follow the Fermi-Dirac distribution of the reservoir. However, as outlined in Chapter 3, the energy level is spin-degenerate. In that case, the distributions depend on the initial occupation of the energy level. If the level is initially occupied, p_1 is given by

$$p_1(E) = \frac{1}{1 + \frac{1}{2}\exp\frac{-E}{k_B T}}, \tag{4.3}$$

which corresponds to a shift of $-k_B T \ln 2$. If it is initially unoccupied, it is instead given by

$$p_1(E) = \frac{1}{1 + 2\exp\frac{-E}{k_B T}}, \tag{4.4}$$

corresponding to a shift of $+k_B T \ln 2$. Both configurations have been used in this thesis. The initial setpoint for all further experiments is when $p_1 = 0.5$,

meaning $E_0 = \pm k_B T \ln 2$.

Spin degeneracy is the cause of one further nuance of the system. So far, only the states $n = 0$ and $n = 1$ have been considered. Spin allows for one more degree of freedom in the state which represents the energy level being occupied by one electron. In the case where the energy level is initially empty, the $n = 1$ can be split up into the $\uparrow$ and $\downarrow$ states, with $p_\uparrow = p_\downarrow = 0.5p_1$. For the other configuration, the split occurs for the $n = 0$ state.

1.3 Entropy production

Recall that that the change in total entropy ΔS_{tot} has two components: one due to heat flow to the environment ΔS_{env} and one to account for the entropy change of the system itself, ΔS_{sys}. Since the heat Q_r can be determined for every trajectory, so can ΔS_{env} which is simply

$$\Delta S_{env} = \frac{Q_r}{T} \tag{4.5}$$

as usual. Following Chapter 2, the entropy change of the system is

$$\Delta S_{sys} = k_B \ln \frac{p_{n(0)}(0)}{p_{n(\tau)}(\tau)}. \tag{4.6}$$

Here, the nuances of spin degeneracy begin to play a role. Every process studied in the thesis is cyclical, meaning $E(\tau) = E(0) = E_0$. If the system was non-degenerate, each state would be equally likely at both $t = 0$ and $t = \tau$ and $\Delta S_{sys} = 0$ for every trajectory. However, since one of the states can be split up into the two spin states, there are actually three states that don't all have the same probability. For trajectories where $n(0) = n(\tau)$, ΔS_{sys} is obviously still zero. On the other hand, if n is different at each end of the trajectory, $\Delta S_{sys} = \pm k_B \ln 2$. Recalling that the difference in internal energy over the trajectory is $\Delta E = (n(\tau) - n(0))E_0$, one can use the first law of thermodynamics to identify the total entropy production as

$$\Delta S_{tot} = -\frac{W_{ex}}{T}. \tag{4.7}$$

1.4 Determining the lever arm

From the above sections, it is clear that to fully describe the trajectories it is necessary to have information about the time evolution of the quantum dot energy level $E(t)$. In order to know that, one must know the lever arm α between

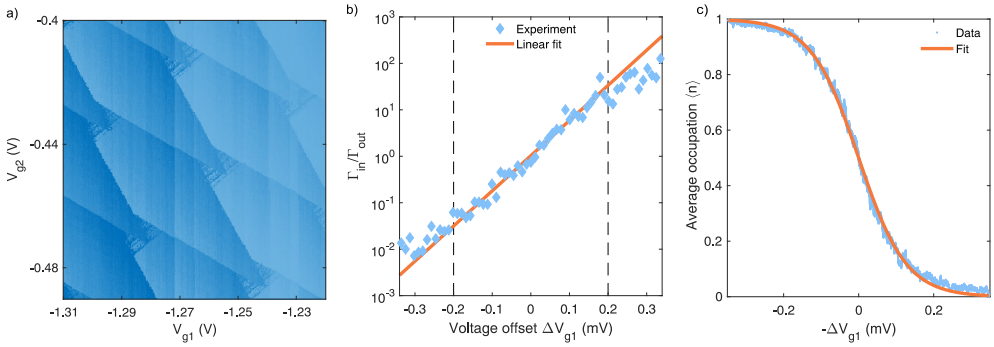

Figure 4.3: Illustrations of different ways to determine the lever arm α. a) DQD charge stability diagram taken with the detector signal at detector bias $V_b = 0.5$ mV. The size of the finite bias triangles can be used to determine the lever arm for all pairs of QD and plunger gate. b) The tunnel rates follow detailed balance given by $\Gamma_{in}/\Gamma_{out} = 0.5\ \exp(\alpha\Delta V_{g1}/k_BT)$. Plotted are both the ratio of the tunnel rates as well as a linear fit to their logarithm. For higher energy offsets, the lowest tunnel rate will be overestimated due the finite measurement length. For that reason, the fit is taken between the two dashed lines. c) Performing roughly 1000 trajectories of the energy level being driven while recording the QD occupation allows for the construction of $\langle n(E)\rangle = \langle n(-\alpha\Delta V_{g1})\rangle$. The data is then fitted to the equilibrium probability distribution to obtain α.

the applied gate voltage and the energy level shift. Over the course of the experiments performed in this thesis, three methods of determining α have been used, summarized in Figure 4.3. Before moving on to summarizing the remaining papers, these three methods will be briefly reviewed.

The first method is the one described in section 2 of Chapter 3. Sweeping both plunger gates of the DQD while applying a bias voltage allows for the construction of a charge stability diagram with finite bias triangles. α can then be determined from the size of the triangles. Notably, the experiments need to be run in a regime where the current in the finite bias triangles is too low to be measured. Therefore, the charge stability diagram needs to be constructed with the charge detection signal as in Figure 4.3a).

The second method involves measuring the tunnel rates for a charge state transition, like in section 4.2 of Chapter 3. That is in any case a necessary step in order to theoretically describe the system. The tunnel rates obey a detailed balance condition so that $\Gamma_{in}/\Gamma_{out} = 0.5\ \exp(-E/k_BT) = 0.5\ \exp(\alpha\Delta V_{g1}/k_BT)$. Depending on the initial occupation of the spin-degenerate level, the pre-factor may also be 2. Performing a linear fit of $\ln\Gamma_{in}/\Gamma_{out}$ as in Figure 4.3b) allows for the extraction of α in terms of k_BT.

Finally, the most time consuming method is to perform many sufficiently slow drives of $E(t)$ and fit the average population $\langle n(\Delta V_{g1})\rangle$ to the equilibrium population probabilities given by equation (4.3) or (4.4). This fit (shown in Fig-

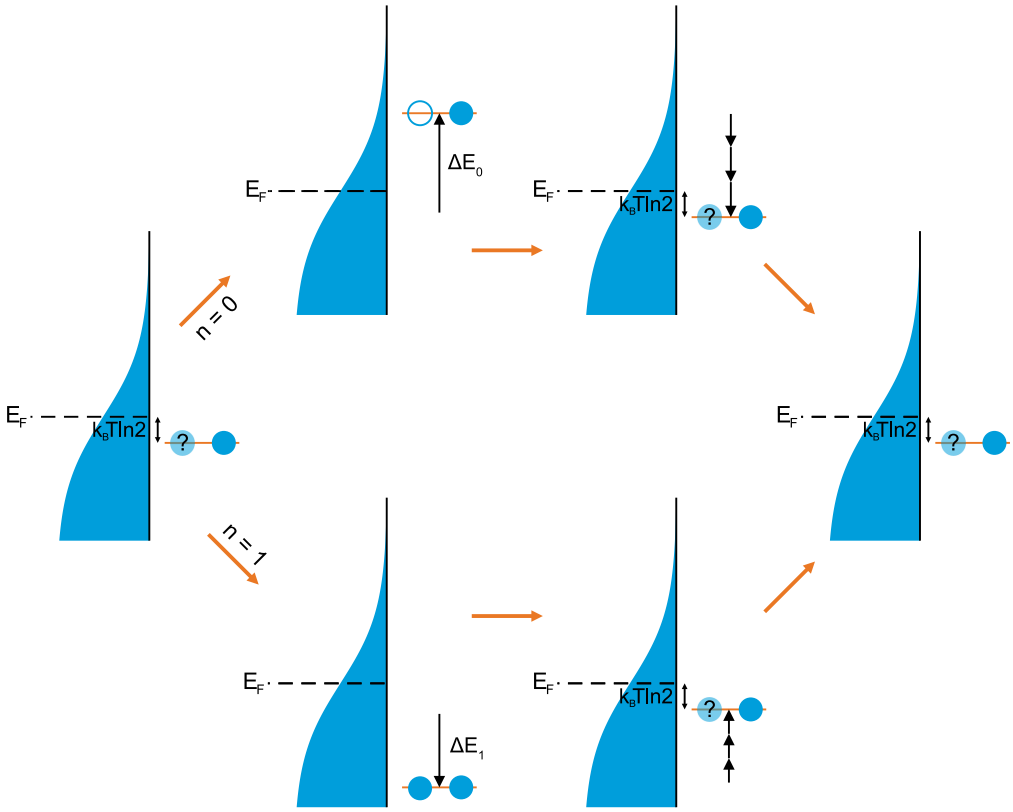

Figure 4.4: Sketch of the Szilard engine operation. There are two possible drives, depending on which state is measured at the start. The single arrows in the second step indicate a fast quench while the stacked arrows in step three mean the level is slowly driven down. At the end, the system has returned to its initial state.

ure 4.3c)) again allows for the determination of α in terms of k_BT.

2 Experimentally realized Szilard engine

In both Paper II and Paper IV, the device is operated as a Szilard engine. This section explains how the conceptual single-particle gas engine introduced by Szilard is translated into one that is experimentally realizable with quantum dots. An overview is given in Figure 4.4.

The system is originally set so that the level has a probability $p_1 = 0.5$ of being occupied by an extra electron. As outlined in the previous section, this occurs when the level is offset from the reservoir Fermi energy by $E_i = k_BT \ln 2$. A measurement of the occupation n thus gives one bit of information which will be

used as the engine's fuel. Measuring n is analogous to measuring on which side of the box the particle is located in Szilard's original thought experiment. The outcome of the measurement determines which type of feedback will be applied to the system. Practically, this is done by routing the detector current to an Arduino DUE microcontroller which compares it to a predetermined threshold. If the current is below the threshold, the system is judged to be in the $n = 0$ state and the microcontroller's analog output is used to perform the drive shown in Figure 4.2. First, E is quickly driven to $E_i + \Delta E_0$. At higher energies $p_0 \to 1$, almost locking the system in the $n = 0$ state. Since the level is unoccupied, this drive can be performed at no work cost. The step of letting the gas do expansion work is realized by slowly lowering E back to the initial point. During this step, electrons can tunnel back and forth between the quantum dot and the reservoir, letting n fluctuate and extracting work W_{ex} as in equation (4.1). As long as there is no measurement error, $W_{ex} \geq 0$ for every trajectory. In the case where initially $n = 1$, another feedback process is applied where E is first quickly lowered and then slowly driven up.

3 Work fluctuation-dissipation relation (Paper II)

Since $n(t)$ is a fluctuating quantity, so is the extracted work W_{ex}. The aim of Paper II was to study the fluctuations in the Szilard engine's work output, and in particular connect them to dissipation through the *work fluctuation-dissipation relation* (FDR). In general, the FDR holds for slowly driven systems where the work distribution is Gaussian and is expressed as

$$W_{diss} = \frac{\sigma_W^2}{2k_B T}, \tag{4.8}$$

where W_{diss} is the dissipated work and σ_W^2 is the work distribution's variance. Before moving to the FDR for the Szilard engine, consider a process where no information is involved. Such a process was realized in Paper II and shown in Figure 4.5. It consists of simply raising the energy level and then lowering it back to its starting point. Recall that for a thermodynamic process, the free energy difference provides a bound for the maximum (on average) extractable work, i.e.

$$\langle W_{ex} \rangle \leq \Delta F. \tag{4.9}$$

For any finite driving speed, equality in Equation 4.9 will not be achieved and some work will be dissipated. The dissipated work can be written as $W_{diss} = \Delta F - \langle W_{ex} \rangle$. For the simple drive from Figure 4.5, $\Delta F = 0$ and $W_{diss} = -\langle W_{ex} \rangle = \langle W \rangle$.

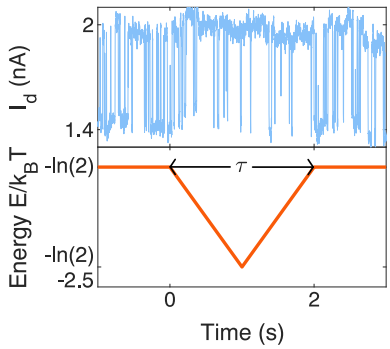

Figure 4.5: Example of a drive which only achieves some dissipation on average. The top panel shows the output of the detector during the drive and the bottom panel shows the drive itself. It consists of simply driving the energy level down by $2.5k_BT$ before driving it up to its initial position.

To test Equation (4.8) experimentally, many trajectories of performing the process were recorded for a variety of different total driving times τ. This allowed for the construction of work distributions shown in Figure 4.6. In those figures, both $\Delta F = 0$ and $\langle W \rangle$ are marked. Clearly, as the drive is slowed down, two things happen. First, the work distribution becomes sharper, meaning fewer fluctuations. Second, the average work moves closer to 0, indicating lower dissipation. The two sides of Equation (4.8) are plotted against each other in Figure 4.7a) and the experimental data does indeed follow the diagonal that indicates equality in the FDR as expected.

Moving on to the Szilard engine, first remember that for a process with measurement and feedback, Equation 4.9 can be violated. Instead, as outlined in Chapter 2, the bound from the second law can be generalized to

$$\langle W_{ex} \rangle \leq \Delta F + k_B T \langle I \rangle, \tag{4.10}$$

by taking into account the information gained in the measurement. For a Szilard engine with two possible initial system states $x = 0, 1$ and two possible feedback protocols denoted by $y = 0, 1$, I is a measure of the information given by

$$I = \ln \frac{P(x, y)}{P(x)P(y)}. \tag{4.11}$$

Here, $P(x, y)$ indicates a probability distribution over initial system state and applied protocol. Over many trajectories, I averages to the mutual information $\langle I \rangle$ between x and y. In the experiment, there is a measurement error rate of around 2%, which affects the measured I. However, in Paper II, the data is

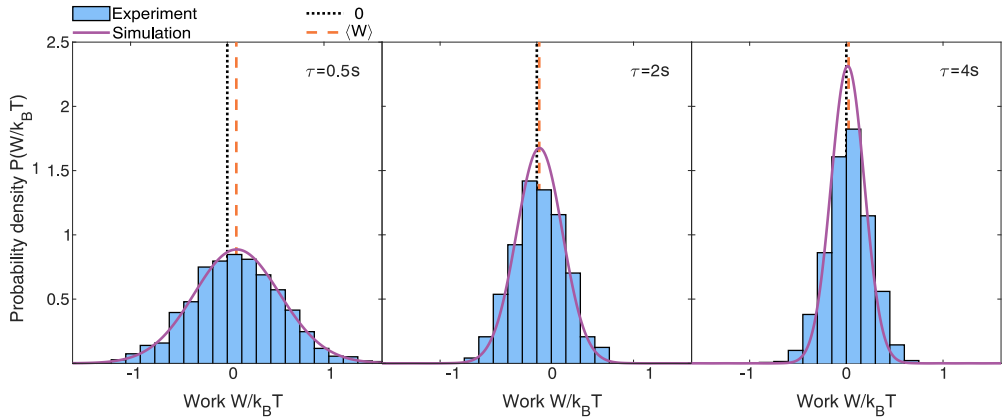

Figure 4.6: Example work distributions for the protocol shown in Figure 4.5. From left to right, the total drive time increases from 0.5 s to $4s$. The average work dissipated is indicated by the orange dashed line. The blacked dotted line is shown at 0 to help guide the eye. For longer drives, less work is dissipated while the distribution also is sharper, in accordance with theoretical simulations shown in purple.

selected to only include successful trajectories. This was done in order to be able to focus only on the shape of a single-peak work distribution. In that case, $I = \ln 2$ for every trajectory and the bound in Equation (4.10) simplifies to the Landauer limit $\langle W_{ex} \rangle \leq k_B T \ln 2$ (keeping in mind that $\Delta F = 0$). Similarly to the case where no information was used, the dissipated work can then be defined as $W_{diss} = k_B T \ln 2 - \langle W_{ex} \rangle$.

Distributions of extracted work were constructed (see Figure 4.8) for Szilard engine implementations with different ramp times τ. For the very fastest drives, the distribution is not Gaussian and there is a big peak near $W_{ex} = 0$ which correspond to trajectories where there was not enough time for any electron tunneling to occur. For slower drives, on the other hand, the distribution moves away from 0 and takes on a more Gaussian shape which gets sharper as the drive time is increased. As the drive is slowed down, the average work $\langle W_{ex} \rangle$ is closer to the Landauer limit, which indicates less dissipation. Figure 4.7b) shows that for fast drives, Equation (4.8) is not obeyed (unsurprisingly since the work distribution is not Gaussian). On the other hand, slower drives stick to the diagonal indicating equality.

The main result of Paper II is summarized in Figure 4.9. It shows both sides of Equation (4.8) plotted against each other for all the different realizations of the experiment. Purple diamonds correspond to quantities from the Szilard engine case while blue points (the different shape indicate a different amplitude was used for the driving) correspond to the protocol where no information was

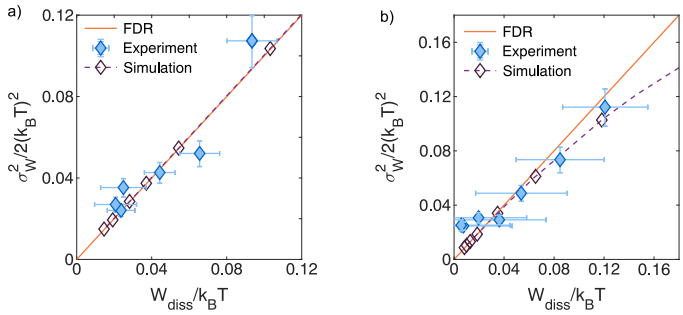

Figure 4.7: The two quantities in the work fluctuation-dissipation relation plotted against each other for a) the dissipative drive and b)the Szilard engine. The orange line indicates equality in the relation. The empty purple diamonds are corresponding theoretical simulations.

used. If you take into account the information content when considering the dissipated work, the FDR is clearly valid for slowly driven Szilard engines just like for processes without feedback.

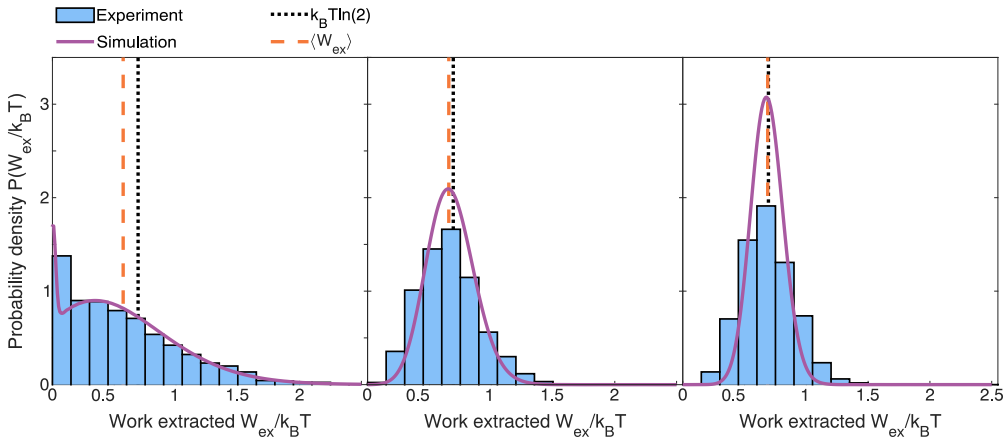

Figure 4.8: Distributions of extracted work for the Szilard engine. In the left panel, the total drive time was 0.25 s, resulting in a non-Gaussian distribution. For the slower drives in the middle (2 s) and right panels (5 s), the distribution tends to a Gaussian and sharpens up as the mean (dashed orange line) moves closer to the Landauer limit (dotted black line).

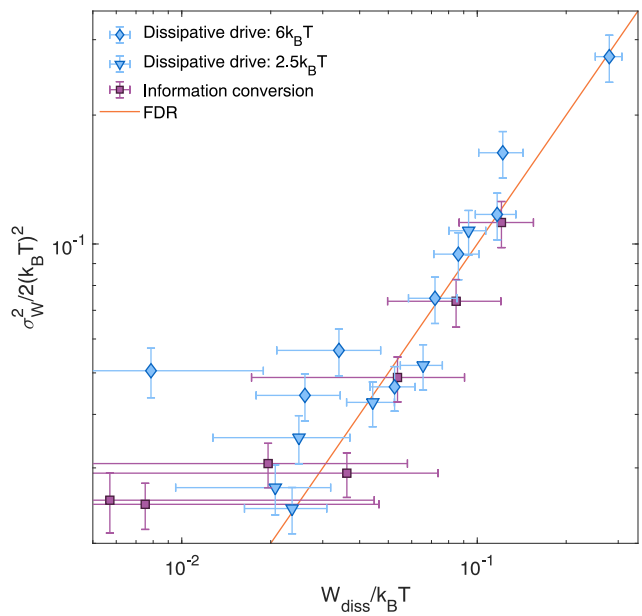

Figure 4.9: The work fluctuation-dissipation relation quantities plotted against each other for all tested protocols. There is a clear tendency to follow the equality line given by the orange diagonal.

4 Optimal driving protocols (Paper III)

Paper III continues on the same track as Paper II, namely experimental studies of dissipation in thermodynamic processes involving information. It is clear that one way to minimize dissipation is to simply perform the drive slowly over a long time. After all, an infinitely slow drive would correspond to a reversible, dissipation-less process. In most practical situations, long timescales are not preferable. One option to performing a slower drive is to change the shape of the drive itself. This alternative is explored in Paper III.

The paper uses the same device as described in earlier sections, but this time it is not operated as a Szilard engine. Instead, the opposite process is used: information erasure. Note however that the same arguments hold for the drive shape in a Szilard engine. The erasure process is as follows: first, the energy level E is set in a high-entropy state so that $p_0 = 0.5$. It is then driven up in energy by the drive amplitude E_A for a time τ. During the drive, p_0 increases and the system is left in a lower-entropy state. It is then quickly brought back down in order to reset the energetics of the system. A measurement of the state immediately after the drive (before it has time to thermalize to equilibrium) would yield less information than a measurement before the drive. In the limit where E_A is high, $p_0(\tau) \to 1$ and the information contained in the system at the start is completely erased.

As described in Chapter 2, such an erasure of information can not be done without some dissipation. In fact, the average heat dissipated is bounded by the Landauer limit:

$$\langle \Delta Q_r \rangle \geq -k_B T \Delta S_{sys}. \tag{4.12}$$

In Paper III, this dissipation was measured for two different drive shapes: the naive linear drive and a, in theory, drive with minimal dissipation called a *geodesic drive*. The idea behind the geodesic drive is to find a shape in which the dissipation occurs uniformly over the trajectory. Intuitively, it makes sense that a minimally dissipative protocol would involve driving slowly while many tunneling events occur (i.e. near the start) and then speeding up to avoid high-energy heat exchange with the reservoir, as shown in Figure 4.10. The exact shape of the drive depends on E_A, with there being a larger deviation from the linear case for large amplitudes.

Experimentally, many trajectories were recorded for both geodesic and linear drives with E_A between $2.6k_BT$ and $10.4k_BT$. For every case, two different drive times were used. In the fast driving case the full drive happened in $\tau = 70$

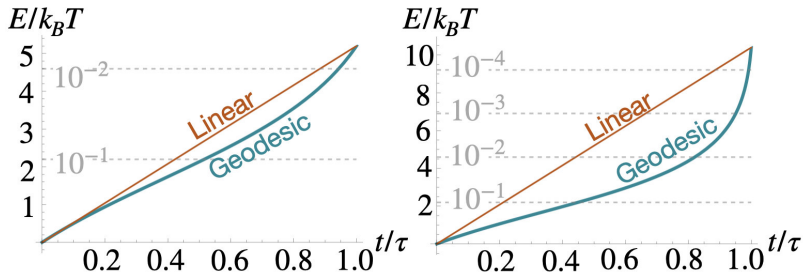

Figure 4.10: Comparison between the linear and geodesic drives used in Paper III. In the left panel, the drives are shown for a drive amplitude of $E_A = 5.2k_BT$ and in the right it is $10.4k_BT$. The larger the amplitude is, the bigger is the deviation between the two shapes.

ms while in the slow driving case the system was driven for $\tau = 1$ s. The heat for each trajectory was determined using equation (4.2). Having full knowledge of the system during the trajectory also allows for the determination of the average heat dissipated over time. An example for $E_A = 10.4k_BT$ is shown in Figure 4.11. As intended, the geodesic drive yields a more uniform dissipation rate than the linear (which spikes early). Note that for even slower drives, the rate is expected to be even more uniform.

In order to compare the performance of each drive shape, two metrics were considered. First was obviously the average heat dissipated ΔQ_r, which is plotted in the right-hand panels of Figure 4.12. These plots show the advantage of the geodesic drive for large drive amplitudes. As the amplitude is increased, the linear drive starts linearly dissipating more heat while the geodesic drive's dissipation saturates. However, less dissipation is not enough if the intended result of the process (i.e. the erasure of information) is not achieved. To quantify the quality of the erasure, the left plots of Figure 4.12 show the percentage of trajectories where $n = 0$ in the end. For perfectly erased information, that quantity would reach 100%. In the slow driving regime, there is no real difference in the erasure quality, meaning the geodesic drive is clearly an improvement over its linear counterpart. However, if τ is short, the erasure quality is slightly better with the linear protocol. The reason for this is the system is driven so quickly near the end that there is not enough time for it to reach equilibrium. If one were to include some extra time for equilibration after the protocol, the two would again reach similar quality. Thus, in the fast driving regime, there is trade-off between erasure quality, dissipation, and time.

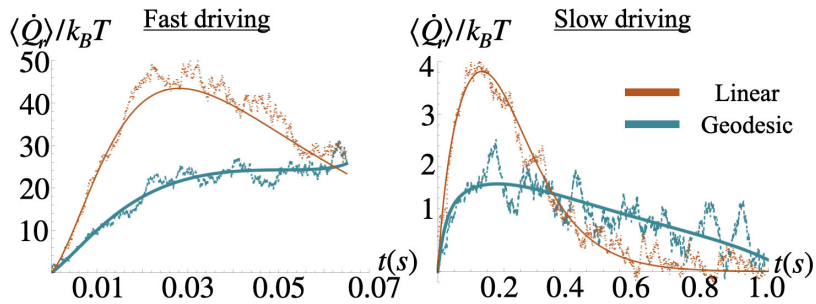

Figure 4.11: Comparisons between the dissipation rates for the two different drive shapes in the fast driving case (left) and the slow driving case (right). The linear drive tends to give a spike in the dissipation rate early on in the drive, whereas the geodesic drive has a more uniform dissipation rate.

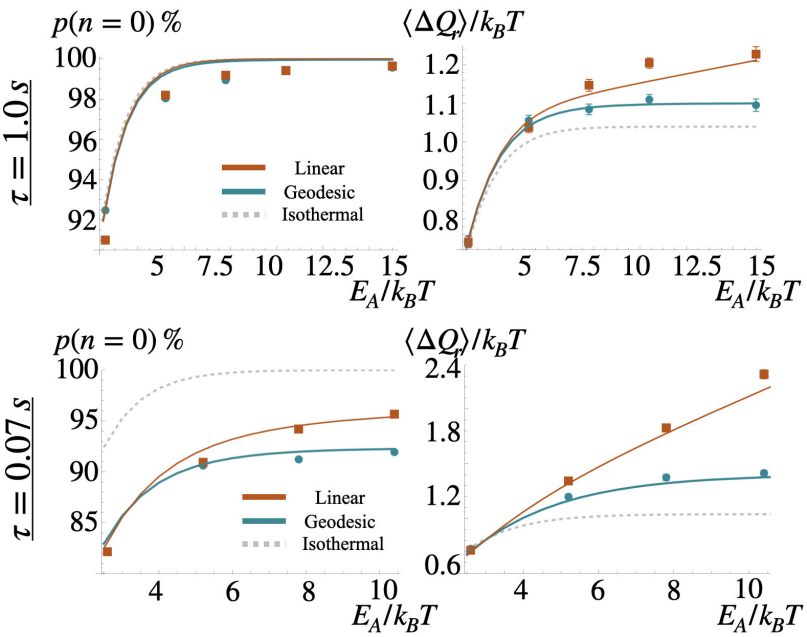

Figure 4.12: Summary of the main results in Paper III. The left panels shows the average population left in the QD after the drive as functions of the drive amplitude, giving a measure of how well the erasure protocol worked. In the slow driving regime, there is no appreciable difference between the two drive shapes. For fast driving, there is a slight decrease when using the geodesic drive. The right panels show the average dissipated heat. For both driving speeds when increasing E_A,the dissipation eventually increases close to linearly with the linear drive while it starts to saturate with the geodesic drive.

5 Thermodynamic uncertainty relations for feedback processes (Paper IV)

Finally, Paper IV deals mainly with the new class of cost-precision trade-off relations known as thermodynamic uncertainty relations (TURs), specifically in the context of the Szilard engine. Recall from Chapter 2 that for systems out of equilibrium, the signal-to-noise ratio of their observables are constrained by their entropy production. For a system that extracts work W_{ex}, the TUR can be expressed as:

$$\frac{\langle W_{ex}\rangle^2}{\sigma_W^2} \leq \frac{\langle \Delta S_{tot}\rangle}{2k_B}, \tag{4.13}$$

with the constraint that the entropy produced $\langle \Delta S\rangle$ is positive. As seen before, for the quantum dot Szilard engine $\Delta S_{tot} = -W_{ex}/T < 0$ as long as the engine extracts work, so Equation (4.13) does not provide a meaningful bound. However, it is also possible to run the engine with parameters (for example, a high measurement error rate) such that the extracted work is negative. In that case, the Szilard engine actually violates the TUR as seen in Figure 4.13. This is due to the inherent time-reversal asymmetry of measurement-feedback scenarios. To introduce a time-reversed trajectory, one would need to pick a feedback to apply beforehand. However, in the forward trajectory, the feedback applied depends on the state of the system at $t = 0$ which would correspond to the end of the backward trajectory. Thus, the probability distributions $P(W_{ex}, \Delta S) \neq P(-W_{ex}, -\Delta S)$ whereas the equality is a necessary condition for Equation (4.13) to hold.

As outlined in Chapter 2, a newer class of TURs has recently been developed which work for systems with broken time-reversal symmetry. In Paper IV, the one studied is on the form

$$\frac{(\langle W_{ex}\rangle + \langle W_{ex}\rangle_B)^2}{\sigma_W^2 + \sigma_{WB}^2} \leq 2\left[\operatorname{csch}^2 f\left(\frac{\langle \Delta S_I\rangle + \langle \Delta S_I\rangle_B}{4k_B}\right)\right]^{-1}, \tag{4.14}$$

where $f(x)$ is the inverse function of $x\tanh(x)$ and the B subscript means it is a quantity from a backward experiment. ΔS_I is the entropy production modified by an information quantifier which may also depend on the backward experiment. There is some choice in the design of the backward experiment, and Paper IV illustrates how the choice of backward experiment gives one access to different information quantifiers and different TUR bounds. In addition, any information quantifier can be used in a generalized second law-like inequality on the form of Equation (4.10).

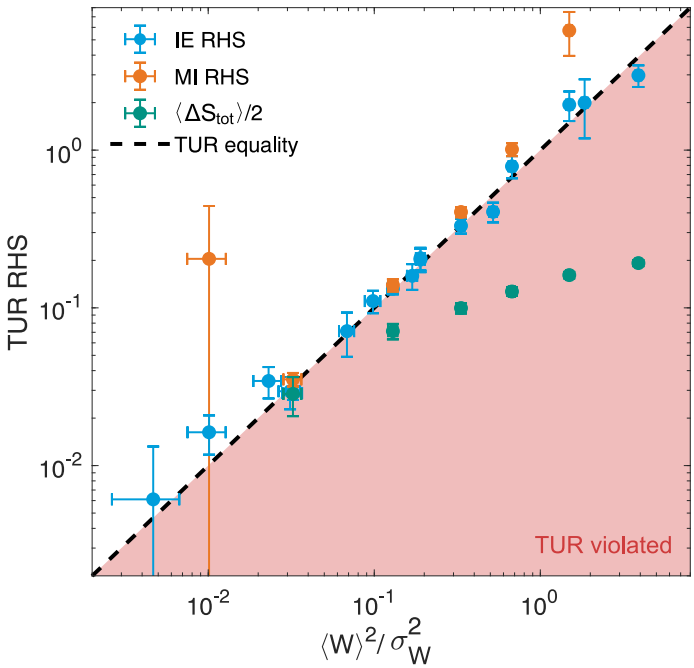

Figure 4.13: The quantities from three different TURs plotted against each other for a Szilard engine operated with a variety of parameters. The green markers show the TUR in Equation (4.13) being clearly violated. The orange and blue markers are from a rearranged version of Equation (4.14) so that the left-hand side is the same as in Equation (4.13). The difference between the two is that they use different backward experiments and information quantifiers. In both cases, they stay close to or above the line which indicates TUR equality.

In Paper IV, two different backward experiments were implemented. Importantly, the probability distributions of the backward experiment must follow a detailed fluctuation theorem which was used in the derivation of Equation (4.14):

$$\frac{P_B(-W_{ex}, -\Delta S_I)}{P(W_{ex}, \Delta S_I)} = e^{\frac{-\Delta S_I}{k_B}}. \tag{4.15}$$

In Figure 4.14, it is shown that the two tested backward experiments do indeed satisfy the fluctuation theorem above with their respective information quantifier. The first backward experiment tested is called the *mutual information* (MI) experiment and was performed as follows: first pick a feedback protocol $y = 0, 1$ and implement it in reverse, so that the slow ramp happens first and the fast quench happens last. Then measure the state of the system immediately after the quench and record it as $x = 0, 1$, which corresponds to the initial state in the forward experiment. This is repeated so that every forward trajectory has a corresponding backward trajectory with the same y. The information quantifier in this case is the quantity I, introduced in Equation (4.11) which averages to the mutual information between x and y in the forward experiment. Note

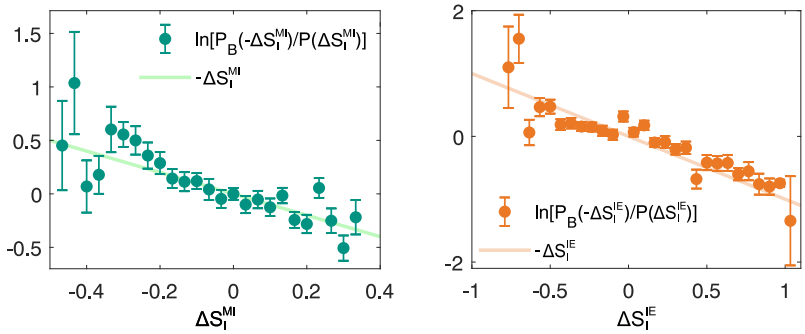

Figure 4.14: After integrating out the extracted work, both the MI (left) and IE (right) backward experiments yield probability distributions of ΔS_I that follow the fluctuation theorem in Equation (4.15), which is shown by the diagonal line.

that for a backward trajectory, $I_B = -I$ is assigned. As shown earlier, this information quantifier provides the second law-like bound of Equation (4.10) which corresponds to the maximum work can that can be extracted using the information from the measurement.

The second backward experiments consists of exactly the same drive as the MI experiment. However, after the drive, the trajectory is discarded unless $x = y$, allowing for some form of feedback to be included in the construction of P_B. One can also include an analogue of measurement error rate by introducing a random variable in the decision to discard the trajectory. In this case, the fluctuation theorem in Equation (4.15) is satisfied with $\Delta S_I = \Delta S - \langle \mathcal{E} \rangle$ where $\mathcal{E}$ is an information quantifier that corresponds to how much entropy production can be inferred if one had access only to the measurement outcomes y:

$$\mathcal{E}(y) = \ln \frac{P(y)}{P_S(y)}, \tag{4.16}$$

where $P_S(y)$ is the probability that a trajectory makes it through the post-selection process. Due to the nature of $\langle \mathcal{E} \rangle$, this backward experiment is called the *inferable entropy* (IE) experiment.

In order to compare the two backward experiments and their respective TURs, two parameters of the Szilard engine operation were varied: the error rate ε (which was implemented by generating a random number in the Arduino script) and how far the energy level is driven after in the $y = 1$ protocol ΔE_1. Figure 4.13 shows that in contrast to the basic TUR, the generalized TUR is not violated for either backwards experiment. Note that Equation (4.14) was rearranged so that the left hand side was identical to the one in the basic TUR. Figure 4.15 shows the same data but plotted as functions of the varied paramet-

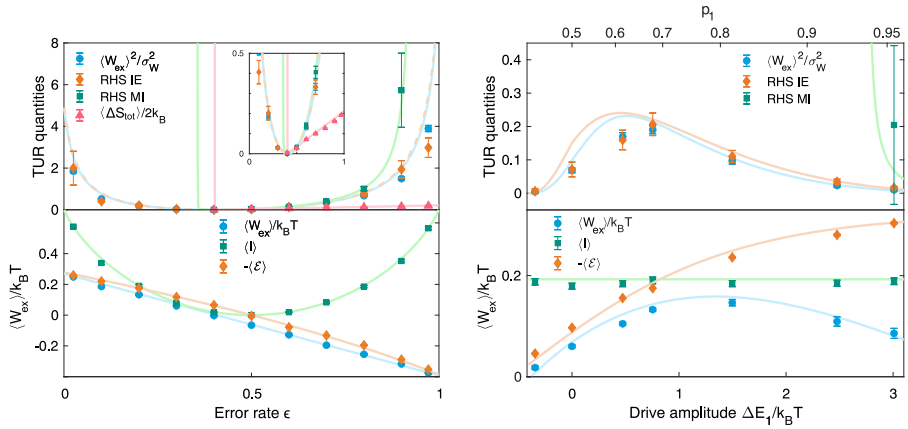

Figure 4.15: Top panels: shows the same TUR quantities as Figure 4.13, but plotted against the error rate with constant drive amplitudes (left) and against the drive amplitude ΔE_1 with a constant error rate and ΔE_0 (right). The inset in the left panel is a zoom-in for small values, showing that when $\varepsilon = 0.5$, all three TURs coincide. Bottom panels: shows the extracted work is bounded by the information quantifiers in a second law-like inequality.

ers instead, showing how the two different backwards experiments lead to qualitatively different TUR bounds. Not surprisingly, when the error rate $\varepsilon = 0.5$ the basic TUR is also satisfied. For that error rate, the engine is just driven randomly and there effectively is no feedback. In addition, the bottom panels illustrate how the extracted work is in all cases bounded by the two information quantifiers.

Chapter 5

Summary and outlook

The interplay between thermodynamics and information is an intriguing subject with a long history that has only quite recently reached the level of experiments. In particular for the process of extracting work from information, the experimental work so far has mainly been concerned with proof-of-concept or reaching high efficiencies. In contrast, the aim of this thesis was to investigate the fluctuations and dissipation involved in information-based processes. In doing so, the thesis work also expanded the experimentally available platforms in the field to include quantum dots formed in semiconductor nanowires.

The first work done for the thesis was establishing the formation of serial double quantum dots (DQD) in InAs nanowires through bandgap engineering. A selectively grown GaSb shell was used to locate the quantum dots using simple imaging techniques, allowing for well-aligned electrical contacts and gates. With DC characterization, it was possible to obtain textbook-like charge stability diagrams, indicating a high degree of control of the DQD charge state. In order to perform real-time measurements of electron tunneling, charge sensing was used. The charge sensing element was a third quantum dot, leading to the somewhat novel device architecture of a system and its detector all integrated in the same nanowire.

The nanowire device was used to experimentally set up the very basic system of a single controllable energy level coupled to a fermionic reservoir, Using the device, a Szilard engine was implemented and work was extracted using information as fuel. This was done in order to investigate the fluctuations in the Szilard engine. First, it was demonstrated that the work fluctuation dissipation relation holds if one takes into account the information gained in a measurement. Then, the new

class of thermodynamic uncertainty relations which present tradeoffs between the precision of processes and their associated entropy production was tested. Depending on how a corresponding backward Szilard engine protocol was constructed, it was possible to define different information quantifiers which came with their own uncertainty relations, fluctuation theorems and second law-like inequalities. Finally, it was shown that by constructing a protocol that distributes its dissipation uniformly along its drive it is possible to minimize the total dissipation. In practice, it was tested for the erasure of information but the same concept can be used to develop optimal drives for the inverse process which is Szilard engine operation.

While this thesis has already shown the range of thermodynamics that can be probed using the quantum dot system, it is still possible to gain even more knowledge using a similar or even the same setup. For instance, the back-action effects described in Chapter 3 for one of the quantum dots are not yet fully understood. However, further measurements and theoretical descriptions could unveil new opportunities to probe non-equilibrium electronic distributions. If one can minimize the back-action effects in both dots (or use a slightly different device architecture), it would be possible to experimentally implement an engine that uses information and feedback to generate a current against a bias. This was first suggested by Averin et al. using single-electron transistors [108], but a version using a double quantum dot engine was proposed by Annby-Andersson et al. in 2020 [109].

The quantum dot system used in this thesis is also a good starting point for experimental investigations of quantum thermodynamics. Quantum thermodynamics and specifically its connection to quantum information is a relatively new field which is growing rapidly together with the development of quantum technology and computing. For systems in which quantum effects such as coherence is generated, many of the thermodynamic relations mentioned in this thesis need to be altered. One example is the fluctuation-dissipation relation studied in Paper II, which in the presence of quantum signatures turns from an equality to an inequality [110]. The double quantum dot allows for the coherent coupling of two discrete energy levels which is a key ingredient for such studies. However, the charge sensing is presently too slow to notice any quantum effects. One way to increase the detection speed is to couple the charge sensing element to a microwave resonator [111, 112]. Work has in fact already begun to couple such resonators to the same type of quantum dot systems in InAs nanowires [113, 114], hopefully further opening up the frontier towards quantum thermodynamics.

References

[1] C. Jarzynski. Equalities and Inequalities: Irreversibility and the Second Law of Thermodynamics at the Nanoscale. *Annual Review of Condensed Matter Physics*, 2:329–351, 2011.

[2] U. Seifert. Stochastic thermodynamics, fluctuation theorems and molecular machines. *Reports on Progress in Physics*, 75:126001, 2012.

[3] C Jarzynski. Nonequilibrium Equality for Free Energy Differences. *Physical Review Letters*, 78(14):2690–2693, 1997.

[4] C. Jarzynski. Equilibrium free-energy differences from nonequilibrium measurements: A master-equation approach. *Phys. Rev. E*, 56:5018–5035, 1997.

[5] Gavin E. Crooks. Entropy production fluctuation theorem and the nonequilibrium work relation for free energy differences. *Phys. Rev. E*, 60:2721–2726, 1999.

[6] Gavin E. Crooks. Path-ensemble averages in systems driven far from equilibrium. *Phys. Rev. E*, 61:2361–2366, 2000.

[7] K. H. Kim and H. Qian. Fluctuation theorems for a molecular refrigerator. *Phys. Rev. E*, 75:022102, 2007.

[8] E.M. Sevick, R. Prabhakar, Stephen R. Williams, and Debra J. Searles. Fluctuation theorems. *Annual Review of Physical Chemistry*, 59(1):603–633, 2008.

[9] J. Liphardt, S. Dumont, S. B. Smith, I. Tinoco Jr, and C. Bustamante. Equilibrium information from nonequilibrium measurements in an experimental test of jarzynski's equality. *Science*, 296(5574):1832–1835, 2002.

[10] D. Collin, F. Ritort, C. Jarzynski, S. B. Smith, I. Tinoco, and C. Bustamante. Verification of the Crooks fluctuation theorem and recovery of RNA folding free energies. *Nature*, 437:231–234, 2005.

[11] G. M. Wang, E. M. Sevick, Emil Mittag, Debra J. Searles, and Denis J. Evans. Experimental demonstration of violations of the second law of thermodynamics for small systems and short time scales. *Phys. Rev. Lett.*, 89:050601, 2002.

[12] D. M. Carberry, J. C. Reid, G. M. Wang, E. M. Sevick, Debra J. Searles, and Denis J. Evans. Fluctuations and Irreversibility: An Experimental Demonstration of a Second-Law-Like Theorem Using a Colloidal Particle Held in an Optical Trap. *Phys. Rev. Lett.*, 92:140601, 2004.

[13] V. Blickle, T. Speck, L. Helden, U. Seifert, and C. Bechinger. Thermodynamics of a Colloidal Particle in a Time-Dependent Nonharmonic Potential. *Phys. Rev. Lett.*, 96:070603, 2006.

[14] O.-P. Saira, Y. Yoon, T. Tanttu, M. Möttönen, D. V. Averin, and J. P. Pekola. Test of the Jarzynski and Crooks Fluctuation Relations in an Electronic System. *Phys. Rev. Lett.*, 109:180601, 2012.

[15] J. V Koski, T. Sagawa, O-P. Saira, Y. Yoon, A Kutvonen, P. Solinas, M. Möttönen, T. Ala-Nissila, and J. P. Pekola. Distribution of entropy production in a single-electron box. *Nature Physics*, 9:644–648, 2013.

[16] B. Küng, C. Rössler, M. Beck, M. Marthaler, D. S. Golubev, Y. Utsumi, T. Ihn, and K. Ensslin. Irreversibility on the Level of Single-Electron Tunneling. *Phys. Rev. X*, 2:011001, 2012.

[17] A. Hofmann, V.F. Maisi, C. Gold, T. Krähenmann, C. Rössler, J. Basset, P. Märki, C. Reichl, W. Wegscheider, K. Ensslin, and T. Ihn. Measuring the Degeneracy of Discrete Energy Levels Using a GaAs/AlGaAs Quantum Dot. *Physical Review Letters*, 117(20):206803, 2016.

[18] A. Hofmann, V. F. Maisi, J. Basset, C. Reichl, W. Wegscheider, T. Ihn, K. Ensslin, and C. Jarzynski. Heat dissipation and fluctuations in a driven quantum dot. *physica status solidi (b)*, 254(3):1600546, 2017.

[19] H. S. Lett and A. F. Rex. *Maxwell's Demon 2: Entropy, Classical and Quantum Information, Computing*. CRC Press, 2002.

[20] R. Landauer. Irreversibility and Heat Generation in the Computing Process. *IBM Journal of Research and Development*, 5(3):183–191, 1961.

[21] C. H. Bennett. Notes on the history of reversible computation. *IBM Journal of Research and Development*, 32(1):16–23, 1988.

[22] T. Sagawa and M. Ueda. Generalized Jarzynski Equality under Nonequilibrium Feedback Control. *Phys. Rev. Lett.*, 104:090602, 2010.

[23] J. M. Horowitz and S. Vaikuntanathan. Nonequilibrium detailed fluctuation theorem for repeated discrete feedback. *Phys. Rev. E*, 82:061120, 2010.

[24] M. Ponmurugan. Generalized detailed fluctuation theorem under nonequilibrium feedback control. *Phys. Rev. E*, 82:031129, 2010.

[25] S. Toyabe, T. Sagawa, M. Ueda, E. Muneyuki, and M. Sano. Experimental demonstration of information-to-energy conversion and validation of the generalized Jarzynski equality. *Nature Physics*, 6:988–992, 2010.

[26] G. Paneru and H. K. Pak. Colloidal engines for innovative tests of information thermodynamics. *Advances in Physics: X*, 5(1):1823880, 2020.

[27] J. V. Koski, V. F. Maisi, J. P. Pekola, and D. V. Averin. Experimental realization of a Szilard engine with a single electron. *Proceedings of the National Academy of Sciences of the United States of America*, 111(38):13786–13789, 2014.

[28] J. V. Koski, A. Kutvonen, I. M. Khaymovich, T. Ala-Nissila, and J. P. Pekola. On-chip maxwell's demon as an information-powered refrigerator. *Phys. Rev. Lett.*, 115:260602, 2015.

[29] M. Rico-Pasto, R. K. Schmitt, M. Ribezzi-Crivellari, J. M. R. Parrondo, H. Linke, J. Johansson, and F. Ritort. Dissipation reduction and information-to-measurement conversion in DNA pulling experiments with feedback protocols. *Physical Review X*, 11(3):031052, 2021.

[30] A. Belabbes, C. Panse, J. Furthmüller, and F. Bechstedt. Electronic bands of III-V semiconductor polytypes and their alignment. *Physical Review B*, 86(7):075208, 2012.

[31] S. Lehmann, J. Wallentin, D. Jacobsson, K. Deppert, and K. A. Dick. A General Approach for Sharp Crystal Phase Switching in InAs, GaAs, InP, and GaP Nanowires Using Only Group V Flow. *Nano Letters*, 13:4099–4105, 2013.

[32] I.-J. Chen, S. Lehmann, M. Nilsson, P. Kivisaari, H. Linke, K. A. Dick, and C. Thelander. Conduction Band Offset and Polarization Effects in InAs Nanowire Polytype Junctions. *Nano Letters*, 17:902–908, 2017.

[33] D. Kondepudi and I. Prigogine. *Modern Thermodynamics: From Heat Engines to Dissipative Structures, Second Edition.* John Wiley Sons, Ltd, 1998.

[34] U. Seifert. Entropy Production along a Stochastic Trajectory and an Integral Fluctuation Theorem. *Phys. Rev. Lett.*, 95:040602, 2005.

[35] J. Hermans. Simple Analysis of Noise and Hysteresis in (Slow-Growth) Free Energy Simulations. *The Journal of Physical Chemistry*, 95(23):9029–9032, 1991.

[36] Douarche, F., Ciliberto, S., Petrosyan, A., and Rabbiosi, I. An experimental test of the jarzynski equality in a mechanical experiment. *Europhys. Lett.*, 70(5):593–599, 2005.

[37] F. Douarche, S. Joubaud, N. B. Garnier, A. Petrosyan, and S. Ciliberto. Work fluctuation theorems for harmonic oscillators. *Phys. Rev. Lett.*, 97:140603, 2006.

[38] C. Jarzynski. Hamiltonian derivation of a detailed fluctuation theorem. *Journal of Statistical Physics*, 98:77–102, 2000.

[39] M. Esposito, U. Harbola, and S. Mukamel. Nonequilibrium fluctuations, fluctuation theorems, and counting statistics in quantum systems. *Rev. Mod. Phys.*, 81:1665–1702, 2009.

[40] A. C. Barato and U. Seifert. Thermodynamic uncertainty relation for biomolecular processes. *Phys. Rev. Lett.*, 114:158101, 2015.

[41] J. Li, J. M. Horowitz, T. R. Gingrich, and N. Fakhri. Quantifying dissipation using fluctuating currents. *Nature Communications*, 10:1666, 2016.

[42] P. Pietzonka, A. C. Barato, and U. Seifert. Universal bound on the efficiency of molecular motors. *Journal of Statistical Mechanics: Theory and Experiment*, 2016(12):124004, 2016.

[43] S. Saryal, H. M. Friedman, D. Segal, and B. K. Agarwalla. Thermodynamic uncertainty relation in thermal transport. *Phys. Rev. E*, 100:042101, 2019.

[44] Andre C. Barato and Udo Seifert. Cost and precision of Brownian clocks. *Phys. Rev. X*, 6:041053, 2016.

[45] A. A. S. Kalaee, A. Wacker, and P. P. Potts. Violating the thermodynamic uncertainty relation in the three-level maser. *Phys. Rev. E*, 104:L012103, 2021.

[46] J. M. Horowitz and T. R. Gingrich. Thermodynamic uncertainty relations constrain non-equilibrium fluctuations. *Nature Physics*, 16:15–20, 2020.

[47] A. C. Barato, R. Chetrite, A. Faggionato, and D. Gabrielli. Bounds on current fluctuations in periodically driven systems. *New Journal of Physics*, 20(10):103023, 2018.

[48] T. Koyuk, U. Seifert, and P. Pietzonka. A generalization of the thermodynamic uncertainty relation to periodically driven systems. *Journal of Physics A: Mathematical and Theoretical*, 52(2):02LT02, 2018.

[49] P. Pietzonka, F. Ritort, and U. Seifert. Finite-time generalization of the thermodynamic uncertainty relation. *Physical Review E*, 96(1):012101, 2017.

[50] P. P. Potts and P. Samuelsson. Thermodynamic uncertainty relations including measurement and feedback. *Physical Review E*, 100(5):052137, 2019.

[51] G. Paneru, S. Dutta, T. Tlusty, and H. K. Pak. Reaching and violating thermodynamic uncertainty bounds in information engines. *Phys. Rev. E*, 102:032126, 2020.

[52] S. Pal, S. Saryal, D. Segal, T. S. Mahesh, and B. K. Agarwalla. Experimental study of the thermodynamic uncertainty relation. *Phys. Rev. Research*, 2:022044, 2020.

[53] L. Szilard. On the decrease of entropy in a thermodynamic system by the intervention of intelligent beings. *Zeitschrift für Physik*, 53:840–856, 1929.

[54] K. Shizume. Heat generation required by information erasure. *Physical Review E*, 52(4):3495–3499, 1995.

[55] B. Piechocinska. Information erasure. *Physical Review A*, 61(6):062314, 2000.

[56] J. M. Horowitz and H. Sandberg. Second-law-like inequalities with information and their interpretations. *New Journal of Physics*, 16(12):125007, 2014.

[57] A. Bérut, A. Arakelyan, A. Petrosyan, S. Ciliberto, R. Dillenschneider, and E. Lutz. Experimental verification of Landauer's principle linking information and thermodynamics. *Nature*, 483:187–189, 2012.

[58] Y. Jun, M. Gavrilov, and J. Bechhoefer. High-precision test of Landauer's principle in a feedback trap. *Phys. Rev. Lett.*, 113:190601, 2014.

[59] M. Gavrilov and J. Bechhoefer. Erasure without work in an asymmetric double-well potential. *Phys. Rev. Lett.*, 117:200601, 2016.

[60] J. Hong, B. Lambson, S. Dhuey, and J. Bokor. Experimental test of Landauer's principle in single-bit operations on nanomagnetic memory bits. *Sci. Adv.*, 2(3), 2016.

[61] L. Martini, M. Pancaldi, M. Madami, P. Vavassori, G. Gubbiotti, S. Tacchi, F. Hartmann, M. Emmerling, S. Höfling, L. Worschech, and G. Carlotti. Experimental and theoretical analysis of Landauer erasure in nanomagnetic switches of different sizes. *Nano Energy*, 19:108–116, 2016.

[62] O. Saira, M. H. Matheny, R. Katti, W. Fon, G. Wimsatt, J. P. Crutchfield, S. Han, and M. L. Roukes. Nonequilibrium thermodynamics of erasure with superconducting flux logic. *Phys. Rev. Res.*, 2:013249, 2020.

[63] S. Dago, J. Pereda, N. Barros, S. Ciliberto, and L. Bellon. Information and thermodynamics: Fast and precise approach to Landauer's bound in an underdamped micromechanical oscillator. *Phys. Rev. Lett.*, 126:170601, 2021.

[64] J. V. Koski, V. F. Maisi, T. Sagawa, and J. P. Pekola. Experimental observation of the role of mutual information in the nonequilibrium dynamics of a maxwell demon. *Phys. Rev. Lett.*, 113:030601, 2014.

[65] L. P. Kouwenhoven, C. M. Marcus, P. L. McEuen, S. Tarucha, R. M. Westervelt, and N. S. Wingreen. Electron transport in quantum dots. In L. L. Sohn, L. P. Kouwenhoven, and G. Schön, editors, *Mesoscopic electron transport*, pages 105–214. Kluwer Academic Publishers, 1997.

[66] C. W. J. Beenakker. Theory of Coulomb-blockade oscillations in the conductance of a quantum dot. *Physical Review B*, 44(4):1646–1656, 1991.

[67] T. Ihn. *Semiconductor nanostructures: quantum states and electronic transport*. Oxford University Press, 2010.

[68] W. G. van der Wiel, S. De Franceschi, J. M. Elzerman, T. Fujisawa, S. Tarucha, and L. P. Kouwenhoven. Electron transport through double quantum dots. *Reviews of Modern Physics*, 75(1):1–22, 2003.

[69] W. J. Parak, L. Manna, and T. Nann. Fundamental Principles of Quantum Dots. In *Nanotechnology*, pages 73–96. American Cancer Society, 2010.

[70] D. Taubert, D. Schuh, W. Wegscheider, and S. Ludwig. Determination of energy scales in few-electron double quantum dots. *Review of Scientific Instruments*, 82(12):123905, 2011.

[71] R. Hanson, L. P. Kouwenhoven, J. R. Petta, S. Tarucha, and L. M. K. Vandersypen. Spins in few-electron quantum dots. *Reviews of Modern Physics*, 79(4):1217–1265, 2007.

[72] D. V. Averin and Y. V. Nazarov. Virtual Electron Diffusion during Quantum Tunneling of the Electric Charge. *Physical Review Letters*, 65(19):2446–2449, 1990.

[73] S. De Franceschi, S. Sasaki, J. M. Elzerman, W. G. van der Wiel, S. Tarucha, and L. P. Kouwenhoven. Electron Cotunneling in a Semiconductor Quantum Dot. *Physical Review Letters*, 86(5):878–881, 2001.

[74] R. Schleser, T. Ihn, E Ruh, K. Ensslin, M. Tews, D. Pfannkuche, D. C. Driscoll, and A. C. Gossard. Cotunneling-mediated transport through excited states in the Coulomb blockade regime. *Physical Review Letters*, 94(20):206805, 2005.

[75] S. Gustavsson, M. Studer, R. Leturcq, T. Ihn, and K. Ensslin. Detecting single-electron tunneling involving virtual processes in real time. *Physical Review B*, 78(15):155309, 2008.

[76] M. Ciorga, A. P. Sachrajda, P. Hawrylak, C. Gould, P. Zawadzki, S. Jullian, Y. Feng, and Z. Wasilewski. Addition spectrum of a lateral dot from Coulomb and spin-blockade spectroscopy. *Physical Review B*, 61(24):R16315, 2000.

[77] J. M. Elzerman, R. Hanson, J. S. Greidanus, L. H. Willems van Beveren, S. De Franceschi, L. M. K. Vandersypen, S. Tarucha, and L. P. Kouwenhoven. Few-electron quantum dot circuit with integrated charge read out. *Physical Review B*, 67(16):161308, 2003.

[78] M. Eich, R. Pisoni, H. Overweg, A. Kurzmann, Y. Lee, P. Rickhaus, T. Ihn, K. Ensslin, F. Herman, M. Sigrist, K. Watanabe, and T. Taniguchi. Spin and Valley States in Gate-Defined Bilayer Graphene Quantum Dots. *Physical Review X*, 8(3):031023, 2018.

[79] S. Sapmaz, P. Jarillo-Herrero, L. P. Kouwenhoven, and H. S. J. van der Sant. Quantum dots in carbon nanotubes. *Semiconductor Science and Technology*, 21:S52–S63, 2006.

[80] C. Fasth, A. Fuhrer, M. T. Björk, and L. Samuelson. Tunable double quantum dots in InAs nanowires defined by local gate electrodes. *Nano Letters*, 5(7):1487–1490, 2005.

[81] S. Tarucha, D. G. Austing, T. Honda, R. J. van der Hage, and L. P. Kouwenhoven. Shell filling and spin effects in a few electron quantum dot. *Physical Review Letters*, 77(17):3613–3616, 1996.

[82] K. Ono, D. G. Austing, Y. Tokura, and S. Tarucha. Current rectification by Pauli exclusion in a weakly coupled double quantum dot system. *Science*, 297(5585):1313–1317, 2002.

[83] C. Stampfer, J. Güttinger, F. Molitor, D. Graf, T. Ihn, and K. Ensslin. Tunable Coulomb blockade in nanostructured graphene. *Applied Physics Letters*, 92(1):012102, 2008.

[84] S. Engels, A. Epping, C. Volk, S. Korte, B. Voigtländer, K. Watanabe, T. Taniguchi, S. Trellenkamp, and C. Stampfer. Etched graphene quantum dots on hexagonal boron nitride. *Applied Physics Letters*, 103(7):073113, 2013.

[85] D. Leonard, M. Krishnamurthy, C. M. Reaves, S. P. Denbaars, and P. M. Petroff. Direct formation of quantum-sized dots from uniform coherent islands of InGaAs on GaAs surfaces. *Applied Physics Letters*, 63(23):3203–3205, 1993.

[86] C. Gatzke, S. J. Webb, K. Fobelets, and R. A. Stradling. In-situ monitoring of the selective etching of antimonides in GaSb/AlSb/InAs heterostructures using Raman spectroscopy. *Semiconductor Science and Technology*, 13:399–403, 1998.

[87] M. S. Gudiksen, L. J. Lauhon, J. Wang, D. C. Smith, and C. M. Lieber. Growth of nanowire superlattice structures for nanoscale photonics and electronics. *Nature*, 415:617–620, 2002.

[88] M .T. Björk, C. Thelander, A. E. Hansen, L. E. Jensen, M. W. Larsson, L. R. Wallenberg, and L. Samuelson. Few-electron quantum dots in nanowires. *Nano Letters*, 4(9):1621–1625, 2004.

[89] P. Caroff, J. Bolinsson, and J. Johansson. Crystal Phases in III – V Nanowires: From Random Toward Engineered Polytypism. *IEEE Journal of Selected Topics in Quantum Electronics*, 17(4):829–846, 2011.

[90] L. Namazi, M. Nilsson, S. Lehmann, C. Thelander, and K. A. Dick. Selective GaSb radial growth on crystal phase engineered InAs nanowires. *Nanoscale*, 7(23):10472–10481, 2015.

[91] D. Barker, S. Lehmann, L. Namazi, M. Nilsson, C. Thelander, K. A. Dick, and V. F. Maisi. Individually addressable double quantum dots

formed with nanowire polytypes and identified by epitaxial markers. *Applied Physics Letters*, 114:183502, 2019.

[92] R. C. Ashoori, H. L. Stormer, J. S. Weiner, L. N. Pfeiffer, S. J. Pearton, K.W. Baldwin, and K. W. West. Single-Electron Capacitance Spectroscopy of Discrete Quantum Levels. *Physical Review Letters*, 68(20), 1992.

[93] M. Field, C. G. Smith, M. Pepper, D. A. Ritchie, J. E. F. Frost, and G. A. C. Jones. Measurements of Coulomb blockade with a noninvasive voltage probe. *Physical Review Letters*, 70(9):1311–1314, 1993.

[94] T. Ihn, S. Gustavsson, U. Gasser, B. Küng, T. Müller, R. Schleser, M. Sigrist, I. Shorubalko, R. Leturcq, and K. Ensslin. Quantum dots investigated with charge detection techniques. *Solid State Communications*, 149(35-36):1419–1426, 2009.

[95] S. Ilani, A. Yacoby, D. Mahalu, and H. Shtrikman. Microscopic Structure of the Metal-Insulator Transition in Two Dimensions. *Science*, 292:1354–1358, 2001.

[96] H. Kiyama, A. Korsch, N. Nagai, Y. Kanai, and K. Matsumoto. Single-electron charge sensing in self-assembled quantum dots. *Scientific Reports*, 8(13188), 2018.

[97] W. Lu, Z. Ji, L. Pfeiffer, K. W. West, and A. J. Rimberg. Real-time detection of electron tunnelling in a quantum dot. *Nature*, 423:422–425, 2003.

[98] R. Schleser, E. Ruh, T. Ihn, K. Ensslin, D. C. Driscoll, and A.C. Gossard. Time-resolved detection of individual electrons in a quantum dot. *Applied Physics Letters*, 85(11):2005–2007, 2004.

[99] S. Gustavsson, R. Leturcq, B. Simovič, R. Schleser, T. Ihn, P. Studerus, and K. Ensslin. Counting Statistics of Single Electron Transport in a Quantum Dot. *Physical Review Letters*, 96(7):076605, 2006.

[100] T. Ihn, S. Gustavsson, U. Gasser, R. Leturcq, I. Shorubalko, and K. Ensslin. Time-resolved charge detection and back-action in quantum circuits. *Physica E: Low-dimensional Systems and Nanostructures*, 42(4):803–808, 2010. 18th International Conference on Electron Properties of Two-Dimensional Systems.

[101] B. Küng, S. Gustavsson, T. Choi, I. Shorubalko, O. Pfäffli, F. Hassler, G. Blatter, M. Reinwald, W. Wegscheider, S. Schön, T. Ihn, and K. Ensslin. Measurement back-action in quantum point-contact charge sensing. *Entropy*, 12(7):1721–1732, 2010.

[102] B. A. Turek, K. W. Lehnert, A. Clerk, D. Gunnarsson, K. Bladh, P. Delsing, and R. J. Schoelkopf. Single-electron transistor backaction on the single-electron box. *Phys. Rev. B*, 71:193304, 2005.

[103] J. Güttinger, J. Seif, C. Stampfer, A. Capelli, K. Ensslin, and T. Ihn. Time-resolved charge detection in graphene quantum dots. *Phys. Rev. B*, 83:165445, 2011.

[104] P. K. Tien and J. P. Gordon. Multiphoton process observed in the interaction of microwave fields with the tunneling between superconductor films. *Phys. Rev.*, 129:647–651, 1963.

[105] L. P. Kouwenhoven, S. Jauhar, J. Orenstein, P. L. McEuen, Y. Nagamune, J. Motohisa, and H. Sakaki. Observation of photon-assisted tunneling through a quantum dot. *Phys. Rev. Lett.*, 73:3443–3446, 1994.

[106] Gloria Platero and Ramón Aguado. Photon-assisted transport in semiconductor nanostructures. *Physics Reports*, 395(1):1–157, 2004.

[107] J. Gooth, V. Schaller, S. Wirths, H. Schmid, M. Borg, N. Bologna, S. Karg, and H. Riel. Ballistic one-dimensional transport in inas nanowires monolithically integrated on silicon. *Applied Physics Letters*, 110(8):083105, 2017.

[108] D. V. Averin, M. Möttönen, and J. P. Pekola. Maxwell's demon based on a single-electron pump. *Phys. Rev. B*, 84:245448, 2011.

[109] B. Annby-Andersson, P. Samuelsson, V. F. Maisi, and P. P. Potts. Maxwell's demon in a double quantum dot with continuous charge detection. *Physical Review B*, 101(16):165404, 2020.

[110] H. J. D. Miller, M. Scandi, J. Anders, and M. Perarnau-Llobet. Work Fluctuations in Slow Processes: Quantum Signatures and Optimal Control. *Physical Review Letters*, 123(23):230603, 2019.

[111] R. J. Schoelkopf, P. Wahlgren, A. A. Kozhevnikov, P. Delsing, and D. E. Prober. The radio-frequency single-electron transistor (RF-SET): A fast and ultrasensitive electrometer. *Science*, 280(5367):1238–1242, 1998.

[112] D. J. Reilly, C. M. Marcus, M. P. Hanson, and A. C. Gossard. Fast single-charge sensing with a rf quantum point contact. *Applied Physics Letters*, 91(16):162101, 2007.

[113] W. Khan, P. P. Potts, S. Lehmann, C. Thelander, K. A. Dick, P. Samuelsson, and V. F. Maisi. Efficient and continuous microwave photoconversion in hybrid cavity-semiconductor nanowire double quantum dot diodes. *Nature Communications*, 12:5130, 2021.

[114] S. Haldar, H. Havir, W. Khan, S. Lehmann, C. Thelander, K. A. Dick, and V. F. Maisi. Energetics of microwaves probed by double quantum dot absorption. arXiv:2208.01323, 2022.